1-1-1979

Effect of impurity elements on hydrogen assisted crack growth in high-strength steels.

Hsi-Cheng Chu

EFFECT OF IMPURITY ELEMENTS ON HYDROGEN ASSISTED CRACK GROWTH IN HIGH-STRENGTH STEELS

by

Hsi-Cheng Chu

A Thesis
Presented to the Graduate Committee
of Lehigh University
in Candidacy for the Degree of
Master of Science
in
Applied Mechanics

Lehigh University

1979

This thesis is accepted and approved in partial fulfillment of the requirements for the degree of Master of Science.

May 31, 1979
(date)

Professor in Charge

Chairman of Department

ACKNOWLEDGEMENT

The author would like to express his gratitude to Professor R. P. Wei, who served as advisor to this research. His leadership and assistance along with personal interest and patience are deeply appreciated. Sincere appreciation is extended to Mrs. Wei for her encouragement. Assistance with the fracture mechanics experiments by Dr. P. S. Pao and Messrs. R. Brazil, G. Shim and C. D. Miller and with scanning electron microscopy by Mr. Douglas Bush is also acknowledged.

Partial support of this research by the National Science Foundation through grant DMR76-21624 is gratefully acknowledged. The author also wishes to express his appreciation to the Air Force Materials Laboratory for providing the AISI 4340 steels and 18Ni maraging steels used in this study; these steels were prepared by the Research Laboratory of the U.S. Steel Corporation under Contract F33615-75-C-5137.

TABLE OF CONTENTS

LIST OF FIGURES

LIST OF TABLES

ABSTRACT

It has been recognized that ultrahigh strength steels are subjected to hydrogen embrittlement. The severity of this embrittlement may be affected by the presence of impurity elements, such as P, S, etc., in these steels. The role of the impurity elements, however, is not well understood. The question is whether they produce a purely mechanical effect or there are chemical interactions with the impurities. To provide additional insight, hydrogen assisted crack growth experiments were carried out on AISI 4340 and 18Ni maraging steels having two different purity levels. The concept of kinetics of crack growth was used for these experiments.

The results indicate that impurities (principally phosphorus and sulfur) in these steels had little influence on Stage II crack growth rates in hydrogen. The impurities produced reductions in the apparent fracture toughness in both classes of steels, and significant reduction in the threshold K (K_{th}) for hydrogen assisted crack growth in the AISI 4340 steel. Based on these results, the principal effect of impurities is considered to be mechanical in nature, and is attributed to the enhancement of crack growth by the increase in non-metallic inclusions (such as MnS in the AISI 4340 steels). The minimal effect of impurities on hydrogen assisted crack

growth in the 18Ni maraging steels is attributed to the significant influence of intermetallic strengthening precipitates that tended to overshadow the impurity effects at the levels used in these experiments.

I. Introduction

It has been recognized that ultrahigh strength steels are subjected to hydrogen embrittlement. The severity of this embrittlement may be affected by the presence of impurity elements, such as P, S, etc., in these steels. The role of the impurity elements, however, is not well understood. The question is whether they produce a purely mechanical effect or there are chemical interactions with the impurities.

McMahon and coworkers [2,3] studied the effects of impurities on temper embrittlement and hydrogen embrittlement in high strength steels. They suggested that temper embrittlement is the result of segregation of impurities to the internal boundaries and thereby reducing the fracture toughness of the steels. They believe that hydrogen embrittlement may follow a similar mechanism, and may in fact combine with temper embrittlement to substantially reduce the stress intensity (K) level required to initiate hydrogen embrittlement (that is, reduce K_{th}). It is not made clear, however, in their work whether this represented a purely mechanical interaction, or there was an additional chemical interaction between hydrogen and the impurity elements (such as phosphorus) in the steels. The crack growth rate data are too scattered to be of value in making this distinction. Furthermore, the steel on which the conclusion regarding impurity effect was based

contained an abnormally low amount of silicon (0.003 w/o vs. 0.25 w/o in normal AISI 4340 steel). Silicon is known to affect tempering response of this class of steels and thereby affect microstructure [4]. As such, the results by these workers may reflect microstructural effects rather than impurity effects alone.

Birkle, et al., [5] showed that the fracture toughness (K_{Ic}) of high-strength steels is affected by sulfur content. They were able to relate this reduction in toughness to the reduction in fracture process zone size [6] which they identified with the average spacing of sulfide (MnS) in the steel. Landes and Wei [7], in their study on creep-controlled crack growth, showed that the rate of crack growth at a given K level is related to the process zone size. As such, the K level required to enforce a given rate of crack growth is reduced with a reduction in process zone size or with an increase in impurity (sulfur) level. The reduction in K_{Ic} and the increased ease in producing subcritical crack growth, therefore, can be related to the increase in sulfide inclusions, and are attributable to purely mechanical interactions with the impurity elements.

Simmons, et al., [8] had analyzed the fracture surfaces produced in hydrogenous environments and showed that the composition of fracture surfaces (principally prior austenite grain boundaries) contained carbon (iron car-

bides), but otherwise was essentially identical with the bulk composition. Segregation of alloying or residual impurity elements to the prior austenite grain boundaries did not appear to be essential for a steel to be susceptible to environment assisted subcritical crack growth, and thus raises a question of possible chemical interaction between hydrogen and the impurity elements.

To resolve these different observations, an experimental program of study is undertaken. This study is premised on the potential influences of impurities on the kinetics of crack growth (Fig. 1) [1], namely in terms of their effects on Stage I (Threshold region), Stage II (K independent) and Stage III (near K_c) of crack growth. The influence of impurity on Stage III crack growth and fracture toughness clearly reflects mechanical interactions. A change in Stage II rates will reflect a change in the chemical driving force and thereby imply chemical interactions of hydrogen and impurities (Fig. 2). A change in the threshold value or Stage I growth (Fig. 3), on the other hand, will reflect a change in both the mechanical and the chemical driving forces. It should be noted, however, that the dominant driving force at Stage I is mechanical. Thus, some resolution of the issue concerning chemical and mechanical interactions may be obtained.

Two materials, AISI 4340 steel and 18Ni maraging steel, were chosen for the study. They represent two

different microstructures and strengthening mechanisms. AISI 4340 steel has a tempered martensite microstructure and uses principally carbon for strengthening. The 18Ni maraging steel has the iron-nickel martensite microstructure, and is age hardened by the precipitation of intermetallic compounds (Ni_3Mo, Fe_2Mo and FeTi). Two different purity levels were selected for each material. Testing was carried out in hydrogen at 133kPa (1000 torr) and room temperature. Previous studies indicate that these conditions would preclude ambiguities in results that might be introduced by pressure-temperature interactions.

II. Material and Experimental Work

A. Material

The steels used in this study were prepared by the Research Laboratory of the United States Steel Corporation under an Air Force sponsored program [9] and were provided to this program by the Air Force Materials Laboratory. These steels were prepared by using a series of vacuum-induction-melting steps followed by a final vacuum-arc-remelting step with prescribed residual impurities, and were cast into 22.9 cm-diameter ingots. The ingots were then forged into approximate 17.8 by 30.5 by 33.0 cm slabs. Each slab was hot-rolled to produce a 2.54 cm thick plate. The plate was then cut into specimen blanks, heat treated and finished to 0.635 cm by surface grinding and then machined into specimens. Chemical composition, heat treatment and mechanical properties for these steels are given in Tables I, II and III, respectively.

B. Specimen and Test Procedure

Wedge opening load (WOL) specimens were used in this study, Fig. 4 [10]. Two slightly different configurations were used. The specimens used for measuring crack growth rates from the Stage I to Stage II transition region into Stage II at constant load (increasing K tests) are as shown in Fig. 4. For measuring crack growth rates into Stage I, tests were carried out under constant crack opening dis-

placement (decreasing K) conditions. These specimens were modified to accept a clip-gage at the specimen edge as shown in Fig. 5. A crack starter notch was introduced into each specimen by electrospark discharge machining (EDM), and the specimen was subsequently precracked by fatigue to introduce a 0.25 cm long crack at the notch tip. Final fatigue precracking was conducted in vacuum at about 10^{-1} Pa at a maximum load equal to about 75% of the anticipated test value [11].

The stress intensity factor expression for the WOL specimen is given by Equation 1, and is accurate over the range $0.3 \leq a/W \leq 0.75$ to ±1% [10].

$$K_I = \frac{P\sqrt{a}}{BW} Y\left(\frac{a}{W}\right) \qquad (1)$$

K_I = Mode I stress intensity factor (Mode I means pure tensile)

P = Applied load (constant)

B = Specimen thickness

W = Specimen width

H = Specimen height = 0.486W

a = Crack length measure from the load line

$$Y\left(\frac{a}{W}\right) = 30.96 - 195.8\left(\frac{a}{W}\right) + 730.6\left(\frac{a}{W}\right)^2 - 1186.3\left(\frac{a}{W}\right)^3 + 754.6\left(\frac{a}{W}\right)^4$$

Both constant load (increasing K) and constant displacement (decreasing K) tests were used. For the con-

stant load (increasing K) tests, load (P) was maintained constant during crack extension to better than ±1% using a closed-loop electrohydraulic test machine operated in load control. Stress intensity factor increased continuously with increasing crack length in accordance with Equation 1. In the constant displacement (decreasing K) tests, load-line displacement (V) was maintained constant during crack extension, to better than ±1% with the aid of an automated closed-loop electrohydraulic test machine operated in displacement control, whereby the load line displacements are continuously converted to crack opening displacements at the specimen edge and used in conjunction with a clip gage to provide control. During a typical test, the applied load decreased with crack growth, and K decreased to K_{th} value as established by the decreased load, Equation 1.

The tests covered a range of K values from about 14 to 60 MPa-$m^{\frac{1}{2}}$. For this range of K levels and for the plate thickness (B) and the yield strength (σ_{ys}) levels employed, the ratio $(K/\sigma_{ys})^2/B$ was less than 0.21[12].

C. Crack Monitoring System

An ac electrical potential system was used for monitoring crack growth in the constant load (increasing K) tests, utilizing a continuous recording system. This system is based on the increase in electrical resistance of the specimen with crack growth. A constant ac current of

1A(rms) was applied to the specimen, and changes in electrical potential were measured between fixed points above and below the crack (Fig. 4). A schematic diagram of the system is shown in Figure 6. Since an analytical relationship between the electrical potential and crack length is not available for the WOL specimen, an experimental calibration curve had to be established. This calibration was accomplished by making simultaneous visual and potential measurements of a growing crack (see Appendix I). From the calibration data the following empirical relationship was obtained by the least squares error method:

$$a = 1.529 + 4.724\ V^* - 1.224\ V^{*2}\ ;\ \text{in cm} \qquad (2)$$

$$\frac{da}{dt} = (4.724 - 2.449\ V^*)\ \frac{1}{V_r}\ \frac{dV}{dt} \qquad (3)$$

The equation was referenced to the potential (V_r) corresponding to the crack starter notch. All of the terms in these expressions are defined in Appendix I in conjunction with details of the data analysis.

For the case of high strength steels tested gaseous hydrogen, however, large deviations have been shown to exist between the actual crack lengths and those indicated by the potential readings [13]. Presumably these deviations are manifestations of the nature of the intergranular fracture process which allows continued electrical contact (or shorting) over much of the crack surface. The correction developed by Landes and Wei and Gangloff [13-15]

to account for this shorting was employed in this investigation. It was assumed that the amount of crack surface in electrical contact is a function of the linear elastic displacement between the crack surfaces. Thus, an estimate of the electrically shorted length can be made and can be applied as a correction to the apparent crack length. The form of this function was empirically chosen. The correction procedure has been verified for several materials under conditions which cause shorting.

In this work a constant current of 1 ampere rms was employed. For the material and instrument setting used, resolution at room temperature was better than 0.003 cm based on 0.1 μV resolution in potential and growth rate resolution of about 6×10^{-8} m/sec. The uncertainty associated with the corrected crack length values was estimated to be ±3%, while the error inherent in individual crack growth rate measurements was about ±20% [15].

A compliance method was used for monitoring crack growth in the constant displacement (decreasing K) test, utilizing a clip gage and a digital computer controlled testing system. This method is based on the change in specimen compliance with crack growth. A schematic diagram of the system is shown in Figure 7. The following equation was used to convert load line displacement (V) into crack length (a) [16], for $0.2 \leq a/W \leq 0.975$ [16].

$$\frac{a}{W} = f(U) = 1.002037 - 5.1122U + 39.4312U^2 - 751.191U^3 + 4929.57U^4 - 10464.7U^5 \quad (4)$$

$$U = [(\frac{BEV}{P})^{\frac{1}{2}} + 1]^{-1}$$

where W = specimen width

B = specimen thickness

E = elastic modulus

Precision in crack length measurement was estimated to be ±1%. Uncertainty in crack growth rates is estimated to be better than ±45% and that for K_{th} to be better than ±15% (see Appendix II).

D. Environment Control System

A gas supply system was used to maintain an ultra-high purity hydrogen environment (see Fig. 8). A stainless steel test chamber (Fig. 9) was bolted to the WOL specimen, and sealed with silicone O-ring seated on both faces of the specimen and within the EDM notch. Dehumidification and purification were accomplished with the aid of the gas train (Fig. 8). Ultra-high purity hydrogen (99.999 pct purity) was passed through a gas purifier (Matheson Model 460 containing Linde 5A molecular sieve, at room temperature) and a cold trap (at -196°C) before admission into the specimen chamber. A cryogenic pump (containing Linde 13X molecular sieve) chilled to -196°C was connected to the discharge side of the specimen chamber and served

as a pump for residual impurities such as CO, CO_2, O_2, H_2O, N_2 and A [17]. Gas discharge was made through a silicone fluid back-diffusion trap. Care was taken to minimize residual impurities by evacuating the system while heating the test chamber and gas supply system to approximately 100°C, and then cooling the traps and cryo-pump before back-filling the system with hydrogen. For tests at pressure 133kPa (1000 torr), hydrogen was allowed to flow continuously through the system with an estimated contamination level of below 1 ppm.

E. Fractography

Characterization of the morphology of fracture surfaces, produced by constant load and constant displacement crack growth tests, were made with the aid of scanning electron microscopy (SEM) to help to identify those microstructural elements or impurities that contribute to hydrogen embrittlement.

The entire broken halves of selected specimens were placed inside an ETEC Autoscan microscope for examination. In this way, the location on the fracture surface can be identified and specific morphological features could be correlated with the stress intensity factor and crack growth rate. The microscope was operated at 20 kV with a working distance of 11 and 16 mm. The specimen was tilted 25° with respect to the incident electron beam, about an

axis parallel to the direction of crack growth. X-ray analysis was used in conjunction with SEM to identify the elemental composition of particles of interest. All fractographs were obtained from areas near the mid-thickness region of the specimens. K values were based on measurements of the distance from the precrack-H_2 crack interface to the area of interest using a precision micrometer stage.

III. Results

Constant load (increasing K) method was used principally to measure Stage II crack growth rates. The data for the two steels at two purity levels are shown and are compared as log $(\frac{da}{dt})$ versus stress intensity factor (K) in Figs. 10 to 15. Least squares analysis of the Stage II data showed that crack growth rate was independent of K on a 95% confidence level basis. The average value of Stage II crack growth rate in hydrogen at room temperature for normal purity AISI 4340 steel was found to be 9.9×10^{-5}m/sec (3.9×10^{-3}in/sec) (Fig. 10) and that for high purity AISI 4340 steel 7.9×10^{-5}m/sec (3.1×10^{-3} in/sec) (Fig. 11). Because of the ±20% scatter in growth rate data from each specimen, there was considerable overlap among the data from the normal and high purity steels. The minimum value of growth rate in the normal purity steel was less than the average crack growth rate for the high purity steel, and the maximum value of crack growth rate in the high purity steel was greater than the average crack growth rate for the normal purity steel. Thus, Stage II crack growth rate for the normal and high purity AISI 4340 steel are considered to be essentially equal (Fig. 12). A similar situation existed in the Stage II crack growth rate data for the normal and high purity 18Ni maraging steels. Average Stage II growth rate for the

normal purity steel was 7.9×10^{-5}m/sec (3.1×10^{-3}in/sec) (Fig. 13) and that for the high purity steel, 4.6×10^{-5} m/sec (1.8×10^{-3}in/sec) (Fig. 14). Again, the Stage II crack growth rates for the normal and high purity 18Ni maraging steels were considered to be essentially equal (Fig. 15).

The decreasing K method was used principally to measure Stage I and K_{th} value. Data were calculated from the load and displacement measurements with the aid of a PDP11/04 minicomputer. After crack arrest has been indicated, the crack opening displacement was maintained constant for at least one hour to ensure that there would be no further crack growth (i.e. at rates greater than the detectability limit of 2.5×10^{-8}m/s). The threshold K value (K_{th}) for crack growth in hydrogen at room temperature for the normal purity AISI 4340 steel was found to be 14.1 MPa - $m^{\frac{1}{2}}$ (12.8 ksi - $in.^{\frac{1}{2}}$) (Fig. 10), and that of high purity AISI 4340 steel was 20.4 MPa - $m^{\frac{1}{2}}$ (18.5 ksi - $in.^{\frac{1}{2}}$) (Fig. 11). An uncertainty of ±15% existed in K_{th} values (see Appendix II). Considering this uncertainty, the difference between these two K_{th} values is considered to be significant (Fig. 12). The corresponding K_{th} values for normal purity 18Ni maraging steel was 17.6 MPa - $m^{\frac{1}{2}}$ (16.0 ksi - $in^{\frac{1}{2}}$) (Fig. 13), and for high purity 18Ni maragins steel at Stage I was 17.1 MPa - $m^{\frac{1}{2}}$ (15.5 ksi - $in.^{\frac{1}{2}}$) (Fig. 14). Based on an uncertainty of ±15%, K_{th}

for the normal and high purity steels are considered to be equal (Fig. 15).

To estimate the K levels associated with Stage III crack growth or the onset of instability, the load required to fracture the specimen in air, after each test, was used. K values were computed by using the failure load the the final crack length from the subcritical crack growth test. Since no further crack growth was considered, each of the K values represents a lower bound estimate of K_c (designated here as K_c^*). K_c^* for the normal and high purity AISI 4340 steel are 69.3 MPa - $m^{\frac{1}{2}}$ (63.0 ksi - $in^{\frac{1}{2}}$) and 135.0 MPa - $m^{\frac{1}{2}}$ (123.0 ksi - $in^{\frac{1}{2}}$), respectively; and for the normal and high purity 18Ni maraging steels, 118.0 MPa - $m^{\frac{1}{2}}$ (107.0 ksi - $in^{\frac{1}{2}}$) and 198.0 MPa - $m^{\frac{1}{2}}$ (180.0 ksi - $in^{\frac{1}{2}}$), respectively. The differences in K_c^* for these two materials, between the normal and high purity conditions, are considered to be significant and to be caused by impurity. These K_c^* values reflect a mixture of opening mode (mode I) and tearing mode (mode III) failure and are therefore larger than the K_{Ic} values. Nevertheless, they indicate that impurity would decrease K_c and K_{Ic}.

In summary, the results indicate that impurities in the steels did not significantly affect Stage II crack growth rates in hydrogen at room temperature. They depressed fracture toughness in both steels, while a de-

crease in K_{th} for crack growth in hydrogen was noted only in the AISI 4340 steel.

Examinations of fracture surface morphology were made by scanning electron microscopy; the various locations for SEM examinations are indicated in Fig. 16. They showed that fracture in hydrogen was predominantly of the "intergranular cracking" type (Fig. 16). The fracture surfaces showed a large amount of intergranular cracking along prior austenite grain boundaries, and small regions of quasi-cleavage and tearing through the prior austenite grains. The tensile overload fracture was predominantly of the "ductile dimple" type.

The fracture surfaces corresponding to K near K_{th} contained a large component of intergranular separation along the prior austenite grain boundaries, deformation markings and apparent phase decohesion on intergranular facets, secondary cracks that apparently follow along prior-austenite grain boundaries, a small amount of quasi-cleavage with respect to the prior austenite grains, and a small amount of ductile tearing (Fig. 17,18). The fracture morphology is similar to that reported for these steels and other iron based alloys, and the susceptibility of prior austenite boundaries to environment induced failures has been observed previously [18-21]. Some inclusions were observed on prior austenite grain boundaries, and areas of quasi-cleavage, and tearing. The characteri-

zation of fracture surfaces for Stage I (Fig. 19,20) and Stage II (Fgi. 21,22) crack growth were the same as that for the K_{th} region. The only difference is that there was a small decrease in the amount of intergranular cracking, and a small increase in quasi-cleavage or ductile tearing, especially in the normal purity steels. In the AISI 4340 steels, the increase in the amount of tearing was greater than that of quasi-cleavage at Stage I and Stage II. In the 18Ni maraging steels, the amount of quasi-cleavage increased more than tearing.

SEM fractographs indicated that the prior austenite grain sizes of the normal purity and high purity AISI 4340 steels were definitely different. Light microscopy was used to examine the microstructure and estimate the prior austenite grain sizes (Fig. 23). The estimated average prior austenite grain sizes were summarized in Table IV. Average prior austenite grain size for AISI 4340 high purity steel was about three times larger than that of the normal purity steel (30.0 μm vs. 12.5 μm). The prior austenite grain sizes were similar in the 18Ni maraging steels.

The fracture surfaces produced by overload were covered entirely by ductile dimples (Fig. 24,25), which formed by microvoid coalescence. Microvoids are initiated at interfaces between the matrix and particles such as caribes and inclusions, and also at imperfections such as

microporosity and microcracks. The shape and depth of dimples, or microvoid, can be related to the size of, and spacing between, initiating particles. The number of particles in the normal purity steels was more than that in the high purity steels.

IV. Discussion

Understanding the influence of steel purity on hydrogen assisted crack growth in ultrahigh strength steels is a complex problem. A number of suggestions concerning the "mechanisms" for the interaction have been proposed in the literature. Results from this study indicated significant influence of impurities (such as sulfur) on the threshold K for hydrogen assisted crack growth (at least in the case of AISI 4340 steel) and on fracture toughness, and minor influence on the rates of Stage II crack growth. These results may be used in assessing the various suggestions and can provide additional insight on the role of the impurity elements in affecting crack growth response. Before the data can be used, however, it is necessary to address the two following experimental issues that directly affect the interpretation of these data. Firstly, for some of the constant displacement tests used in determining Stage I crack growth and K_{th}, the crack deviated from the intended growth direction by up to 15^{o}. This deviation introduced Mode II (forward sliding mode) loading which can affect the apparent K_{th} value and crack growth rate. An estimate of this source of variability is needed in assessing the significance in the observed differences in K_{th} and Stage I rates. Secondly, the contribution from differences in prior austenite grain sizes

for the AISI 4340 steels must be estimated. Once these issues are addressed, considerations of the experimental data can be made.

A. Influence of Crack Plane Orientation

In some of the decreasing K tests, the crack plane was inclined at some angle (β), with respect to the normal crack plane orientation (that is, oriented perpendicular to the loading direction). In these cases, the apparent K_{th} values are not expected to be the same as those for a normal crack, because crack growth should be considered as combined Mode I and Mode II extension. In other words, $K_{th} = f(K_I, K_{II})$. Subcritical crack extension under mixed mode loading in hydrogen has not been studied before. An estimate of its effect may be made by using the concept of strain-energy density factor (S) proposed by Sih [22], if one assumes that the crack driving force in mixed mode might be characterized by S. The solution for an inclined central crack in an infinitely large plate is used in making this estimate [22], see Eq. (5).

$$S_{th} = (a_{11}K_I^2\cos^2\beta + 2a_{12}K_IK_{II}\sin\beta\cos\beta + a_{22}K_{II}^2 \sin^2\beta)\cos^2\beta \qquad (5)$$

$$a_{11} = \frac{1}{16\mu}\,[(3-4\nu-\cos\theta)(1+\cos\theta)]$$

$$a_{12} = \frac{1}{16\mu}\,2\,\sin\theta[\cos\theta-(1-2\nu)]$$

$$a_{22} = \frac{1}{16\mu}[4(1-\nu)(1-\cos\theta) + (1+\cos\theta)(3\cos\theta-1)]$$

$$K_I = K_{th} \cos^2\beta$$

$$K_{II} = K_{th} \sin\beta\cos\beta$$

where K_I and K_{II} are the stress intensity factors for Mode I and Mode II at the tip of the inclined crack, μ is the shear modulus, ν is the Poisson ratio, β is the crack plane orientation, and θ_o is used to define the direction of S_{min} [22]. K_{th} here is to be interpreted as the apparent threshold value that one would compute from the applied stress and the crack length as if the stress were applied normal to the crack plane. The apparent K_{th} for various crack plane orientations (β) are given in Table V, along with the directions (θ_o) for S_{min}. (See also Fig. 28) A comparison of four sets of experimental data (corresponding to $\beta = 0^o$, 8^o, 10^o and 14^o) with the predicted values of apparent K_{th} from Eq. 5, based on data for $\beta = 0^o$ and θ_o obtained from Sih [22], is shown in Fig. 28. The predicted values were slightly less than the experimental data. The difference between the two sets of values may be caused by the fact that Eq. (5) was derived for a center crack under uniform remote tension, which may not be fully compatible with the WOL specimen used in these experiments. The difference may also reflect local crack orientation as determined by the orientation of the prior austenite grain boundaries at the crack tip with respect to the loading axis. In any case, dif-

ferences in crack plane orientation appear to offer a reasonable explanation for the observed scatter in K_{th}, and, more importantly, indicate that the difference between the K_{th} values in normal and high purity AISI 4340 steels is significant.

B. Effect of Prior Austenite Grain Size

The results from the AISI 4340 steel indicate that the high purity steel exhibited a higher K_{th}. But because of the difference in prior austenite grain size, it is necessary to consider what influence this grain size difference might have on the observed difference in K_{th}. One of the possible effects is through the increased concentration of impurities that might segregate on the boundary surfaces. With increases in grain size, the surface to volume ratio decreases. Thus the concentration of impurities is expected to increase with increasing grain size, and would result in a lowering of K_{th}. Increasing grain size would also lead to a decrease in fracture stress, which is proportional to the inverse square root of grain size. This dependence would also suggest a lowering of K_{th} with increasing prior austenite grain size. On the other hand, increasing grain size may result in a reduction in flow (yield) stress, which may cause an increase in K_{th} [23]. Available experimental data [23,24,25] suggest that K_{th} tended to increase with prior austenite

grain size, and thus contradict the first two of the above suggestions. In any case, for the grain sizes considered here (10 to 30 μm) the difference in K_{th} is not large; that is, on the order of 10 percent. These considerations suggest that even if all of the possibilities are applicable, correction for the influence of grain size would tend to lead to a larger difference in K_{th} between the normal purity and high purity AISI 4340 steels than that observed. Thus, the observed difference represents, at least, a lower bound on the impurity effect.

C. Influence of Impurities

Results from increasing K tests of the two different steels at a hydrogen pressure of 133 kPa (1000 Torr) and room temperature showed that the crack growth rates at Stage II are not significantly affected by the presence of impurities in the steels. These results are consistent with those reported by others and with the Stage II growth rates obtained on comparable steels [2, 8, 26, 27]. Using the data of McMahon, et al. [2], for normal purity and high purity AISI 4340 steel at room temperature, extrapolating to 133 kPa hydrogen pressure, one would estimate Stage II rates of about 1.0×10^{-4} m/sec (4.0×10^{-3} in/sec). Simmons, et al. [8], measured Stage II rate in another high purity AISI 4340 steel to be 7.8×10^{-5} m/sec (3.1×10^{-3} in/sec). All of these data are comparable to those ob-

tained in this study. Similarly for high-purity 18Ni maraging steels, Pao, et al. [26], and Gangloff, et al. [27], found crack growth rates at Stage II in hydrogen were comparable (that is, 5.1×10^{-5}m/sec (2.0×10^{-3}in/sec)) to those obtained in this study. These results suggest that there was no chemical interaction between hydrogen and the impurities to affect the chemical driving force for crack growth.

The results from the decreasing K tests showed that K_{th} values for the 18Ni maraging steels were essentially unchanged by steel purity, while those for the AISI 4340 steels were different. The results for the 18Ni maraging steels would tend to suggest that impurity had little effect on either the chemical or the mechanical driving forces at K_{th} and in Stage I. Data on the AISI 4340 steels, on the other hand, indicate a meaningful effect that need to be accounted for through considerations of the metallurgical and mechanical contributions.

Fractographic examinations showed that the fracture surfaces of these two steels exhibited intergranular cracking for the most part at K_{th}. In the 18Ni maraging steels, there was a large component of intergranular separation with a finite amount of transgranular quasi-cleavage. The susceptibility of prior austenite grain boundaries to hydrogen induced failure has already been

documented in several studies [19,28]. It is reasonable to expect that massive martensite lath boundaries would also be susceptible, and that the observed transgranular quasi-cleavage failure would follow along these martensite lath boundaries. Fractographic results would suggest that martensite lath boundaries tend to be less susceptible to hydrogen embrittlement at K_{th}. The only difference between the normal purity and high purity steels is that more inclusions were observed on the fracture surfaces of the normal purity steel. X-ray analysis indicates the presence of Fe, Ni and S in these inclusions (Fig. 26). Since there was no apparent difference in K_{th}, the presence of these inclusions or the segregation of impurities (such as phosphorous) to prior austenite grain boundaries cannot be readily reconciled against the experimental data (that is, an apparent absence of impurity effects).

For the AISI 4340 steel, near K_{th}, the fracture surfaces again contained a large component of intergranular separation along the prior austenite grain boundaries, a small amount of quasi-cleavage, and a small amount of ductile tearing. It is also reasonable to expect transgranular quasi-cleavage to occur along martensite boundaries. Some inclusions were also found on fracture surface, including the prior austenite grain boundaries, martensite lath boundaries and tearing areas. X-ray analy-

sis indicate the inclusions to be composed of Fe, Mn, S and probably MnS (Fig. 27). Some other particles that were present on the fracture surfaces are probably carbides, but could not be identified by X-ray analysis. Because previous discussion and the results on the 18Ni maraging steels suggest that segregation of impurities (such as phosphorous) to the prior austenite grain boundaries could not account for observed difference in K_{th}, an alternative explanation is needed. Birkle, et al. [5], had shown that fracture toughness can be affected by impurity (namely sulfur) in high-strength steels. Its effect can be related quantitatively through correlation with a fracture process zone size (d_T), which can be identified in turn with the average spacing of sulfide inclusions (or other inclusions) in the steel. A more direct identification may be made through considerations of creep-controlled crack growth by Landes and Wei [7]. These workers showed that the crack growth rate at a given K level is a function of K_c, which can be related in turn to d_T.

Specifically, from [7],

$$d_T = \left(\frac{K_c}{\sigma_y\sqrt{\pi}}\right)^2 (0.75\ N\ \varepsilon_y)^{\frac{N+1}{N}} \qquad (6)$$

$$\frac{da}{dt} = S\left(\frac{K_c}{\sigma_y\sqrt{\pi}}\right)^2 (0.75\ N\ \varepsilon_y)^{\frac{N+1}{N}} (N+1)/\left[1 - \left(\frac{K}{K_c}\right)^{\frac{2N}{N+1}}\right] \qquad (7)$$

Combining Eqs. (6) and (7) gives

$$K \propto (d_T)^{\frac{2N+1}{2N}}$$

As a first order approximation, one can identify K_{th} with the K level that would be required to enforce a given rate of crack growth. Thus, one can expect K_{th} to be approximately proportional to d_T or to the average inclusion spacing (that is, $K_{th} \propto d_T = \bar{d}$) for large values of N.

Inclusion spacings were estimated from SEM fractographs of AISI 4340 steels and 18Ni maraging steels at magnifications of 1500X, 3000X and 6000X, and are given in Table VI. The ratio of average inclusion spacings between the high-purity and normal-purity AISI 4340 steel was found to be 1.5 ± 0.7 at the 95% confidence level. This ratio is in good agreement with the ratio of K_{th} of about 1.45 for this steel. The corresponding ratios for the 18Ni maraging steels are 1.3 ± 0.3 for inclusion spacings and 1.0 for K_{th}. These comparisons suggest that the observed influence of impurities resulted from an easing of the mechanical processes of crack growth only, particularly in the AISI 4340 steels, through the introduction of inclusions. The apparent absence of impurity effect in the 18Ni maraging steels may reflect, in part, the sensitivity of measurements and, in part, the overwhelming influence of principal alloying elements [26,27].

This suggestion is consistent with the effect of impurities on the apparent fracture toughness of these steels. The appearance of the overload fracture surfaces is consistent with the model of the growth and coalescence of particle-nucleated voids, which was suggested to be the principal mechanism for crack growth in these steels at room temperature. The normal purity 18Ni maraging steel and AISI 4340 steel fracture surfaces contained more inclusions than those of the high purity steels; some of the inclusions were composed of Mn and S. The suggestion of Birkle, et al. [5], that the different K_c or K_{Ic} values were affected by MnS inclusions is consistent with these observations. The suggestion is also consistent with the observations of Simmons, et al. [8], which showed that there was no segregation of alloying or residual impurity elements at the prior austenite grain boundaries. Thus, the reduction in K_{th} resulted from the presence of increased amounts of inclusions in the less pure steels. In AISI 4340 steel, the difference between normal purity and high purity was associated with MnS inclusions. In the 18Ni maraging steels the effect was overshadowed by other inclusions or precipitates. The segregation of impurities on prior austenite grain boundaries, as suggested by McMahon, et al. [2,3], and the suggested additive effects of impurities and hydrogen on K_{th} do not appear to be reasonable.

CONCLUSIONS

The kinetics of hydrogen assisted crack growth at room temperature and a hydrogen pressure of 133 kPa and the apparent fracture toughness were determined on two classes of high-strength steels and two purity levels to obtain further insight on the role of impurities in these steels on their hydrogen embrittlement and fracture response. The steels include a quenched and tempered, medium-carbon low-alloy steel (AISI 4340 steel) and an age-hardening nickel-martensitic steel (18Ni maraging steel). The principal results are as follows:

1. Impurities lowered the apparent fracture toughness and the threshold K (K_{th}) for hydrogen assisted crack growth in the AISI 4340 steel, but had essentially no effect on Stage II crack growth.
2. Impurities lowered the apparent fracture toughness in the 18Ni maraging steel, but otherwise had little effect on K_{th} or Stage II crack growth in hydrogen.
3. The fracture paths for hydrogen assisted crack growth in both steels followed principally along prior austenite grain boundaries.
4. Nonmetallic inclusions (MnS) were identified on the fracture surfaces of AISI 4340 steels cracked in hydrogen. The ratio of average inclusion spacings for the normal and high purity steels correlated

with the ratio of K_{th} in these steels on the basis of the Landes-Wei model for crack growth.

5. These inclusions were also found on surfaces produced by tensile overload fracture in the AISI 4340 steels. The fracture process here was by inclusion initiated void nucleation and growth. The density of inclusions is consistent with the increase in fracture toughness with purity.
6. Inclusions (containing Fe, Ni and S) were identified on the fracture surfaces of 18Ni maraging steels cracked in hydrogen. No meaningful correlation between inclusion spacing and K_{th} was established in this case.
7. These inclusions and others (probably Ti(C,N) and TiS) were found on the tensile overload fracture surfaces of the 18Ni maraging steels. The density of these inclusions is again consistent with the change in fracture toughness with purity.

These results suggest that there was no significant chemical interaction between impurities and hydrogen. The principal effect of impurities appears to be mechanical in nature, and is consistent with an enhancement of the mechanical process for cracking by the presence of nonmetallic inclusions in the case of AISI 4340 steel. This is consistent with a reduction of K_{th} for hydrogen

assisted cracking by temper embrittlement, and does not depend on additional chemical interaction between hydrogen and second phases that might segregate at prior austenite grain boundaries or other internal boundaries. The apparent absence of impurity effects on hydrogen assisted crack growth in the 18Ni maraging steels is believed to be the result of the dominant influence of strengthening precipitates that segregated at the prior austenite grain boundaries. Additional work at other purity levels are needed to fully explore the influence of impurity elements on hydrogen embrittlement response in high-strength steels.

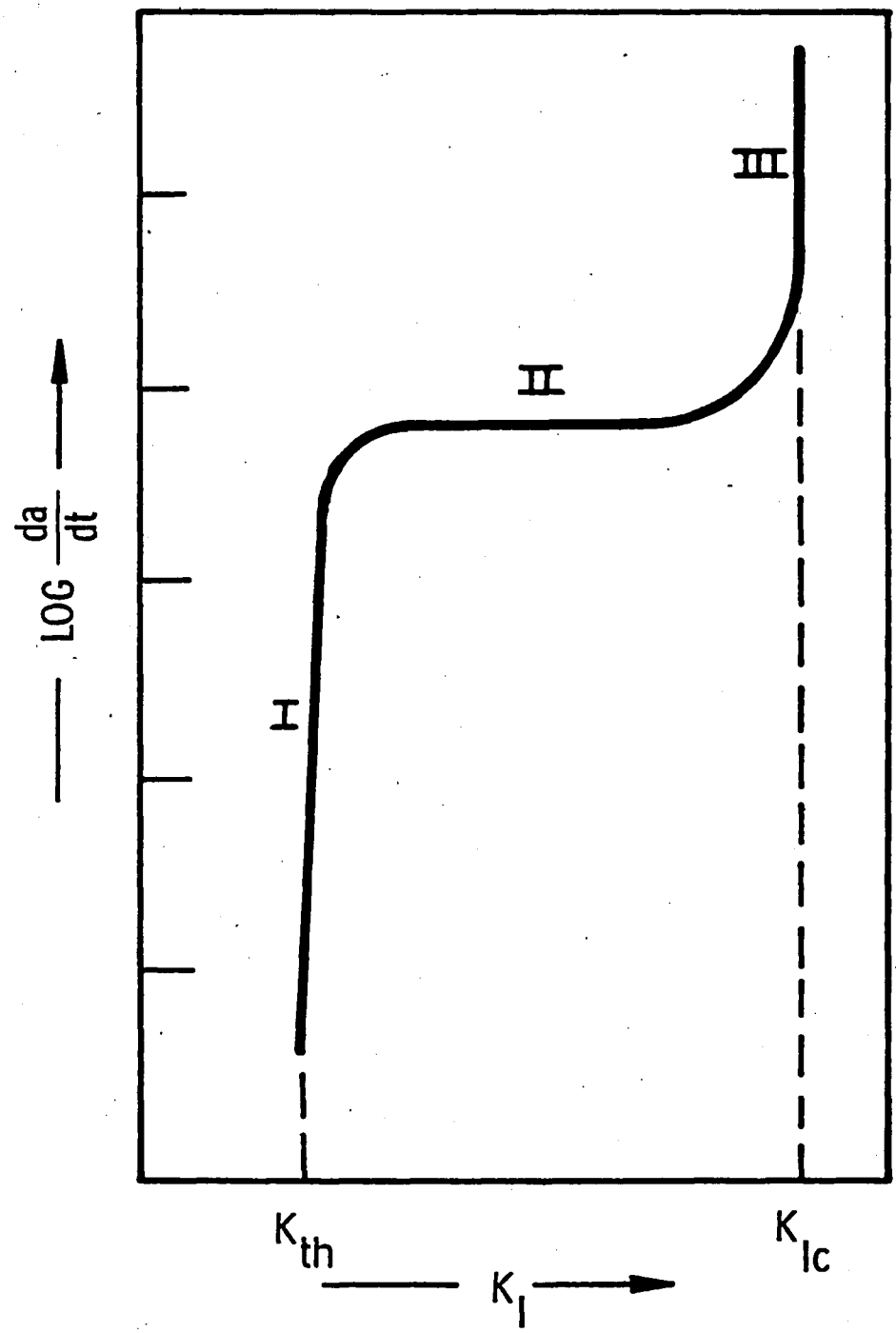

Fig. 1. Schematic of environment enhanced crack growth response.

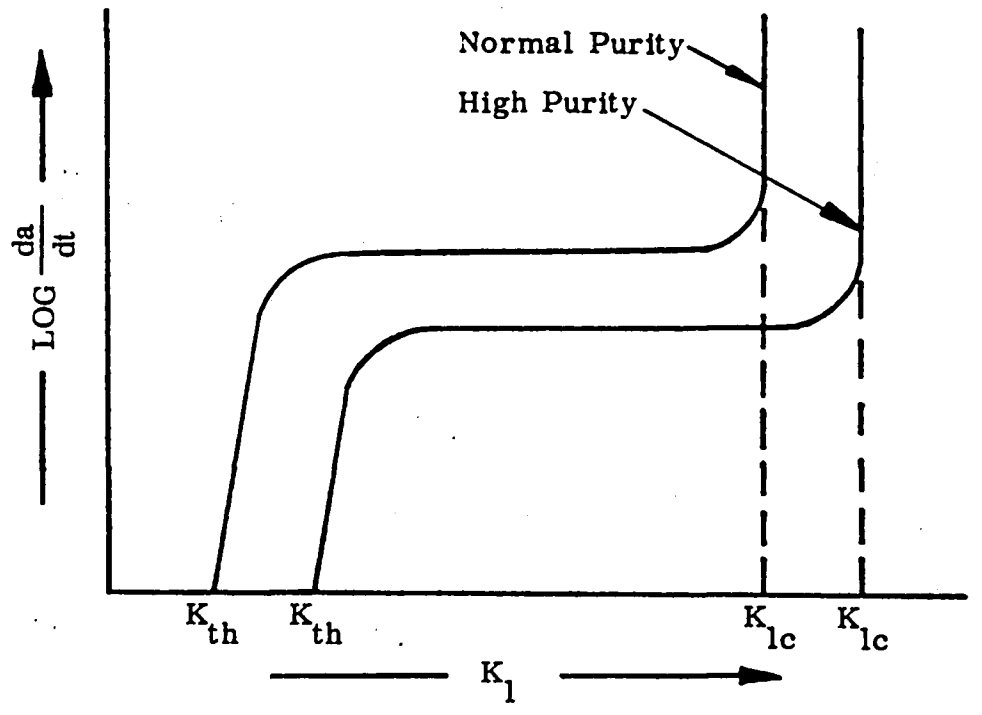

Fig. 2. Schematic of crack growth response where impurity resulted in chemical and mechanical interactions.

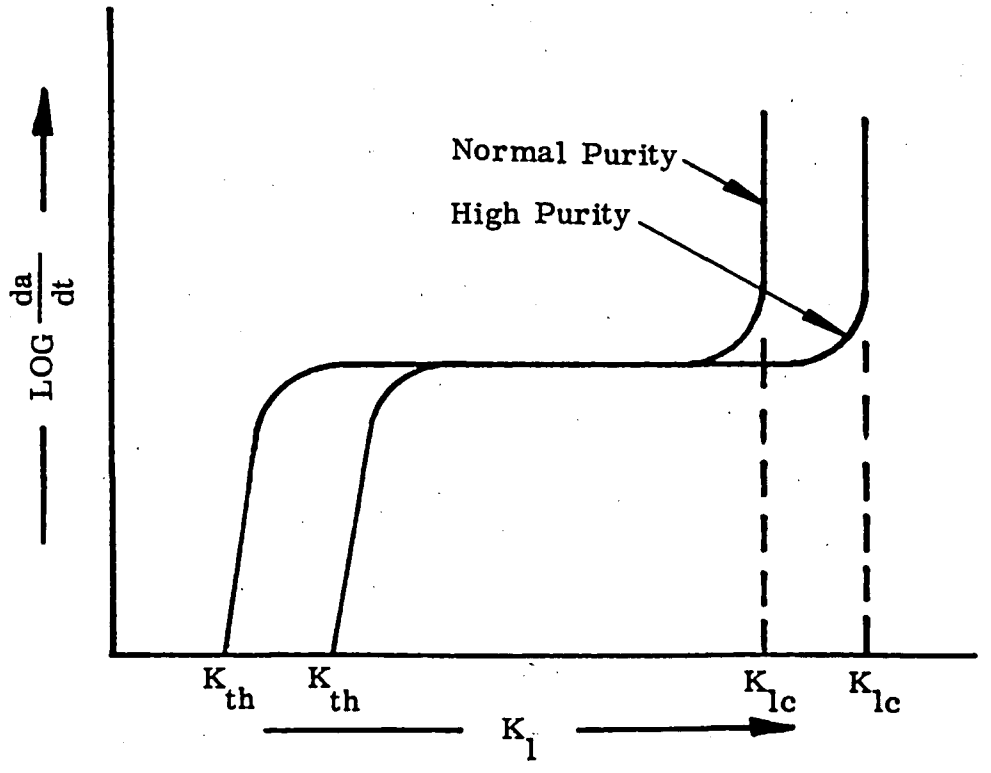

Fig. 3. Schematic of crack growth response where impurity produced only mechanical interactions.

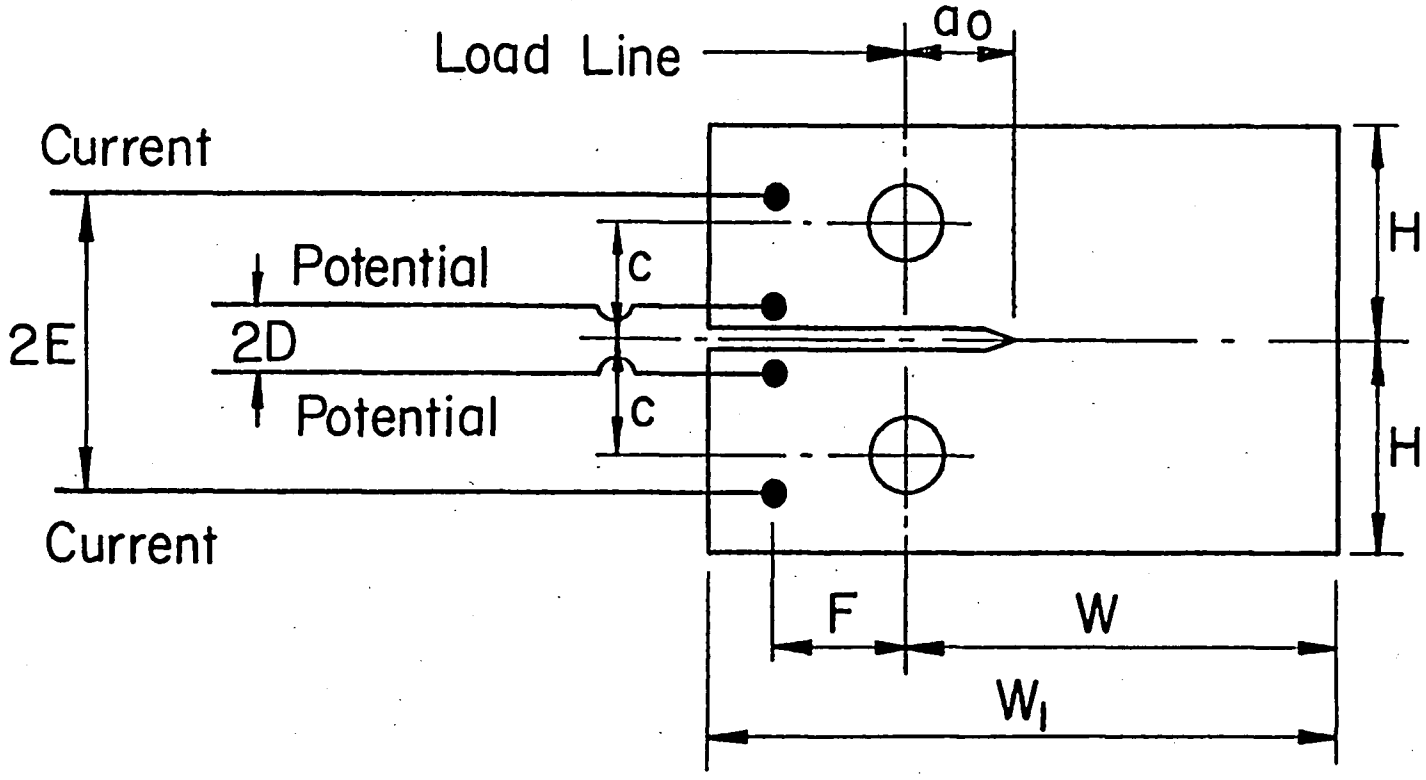

	B*	a	W	H	W_1	C	D	E	F
cm	0.64	1.52	5.23	2.54	7.00	1.40	0.35	1.75	1.40
in	0.25	0.60	2.06	1.00	2.75	0.55	0.14	0.69	0.55

* thickness

Fig. 4. WOL specimen.

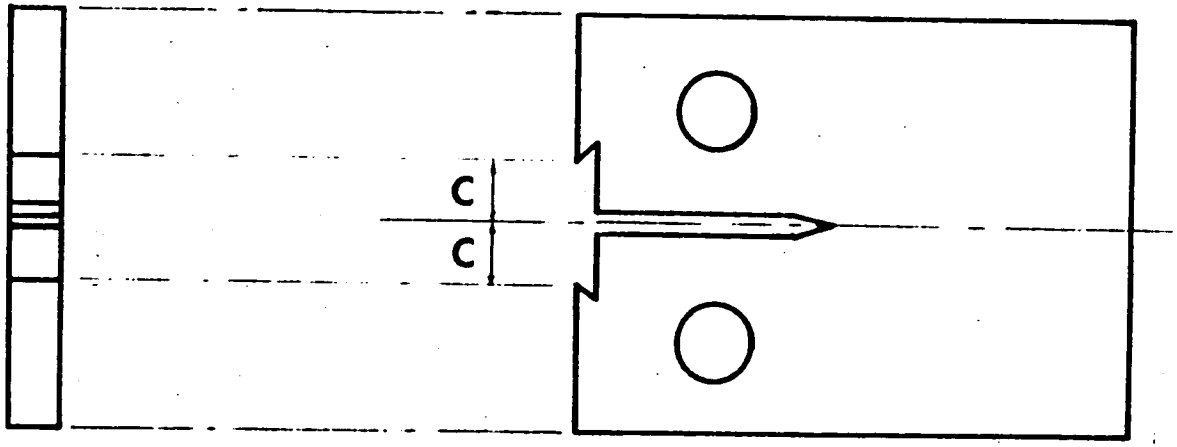

C = 1.45 cm
(0.57 in)

Fig. 5. WOL specimen with clip gage attachment points on one edge.

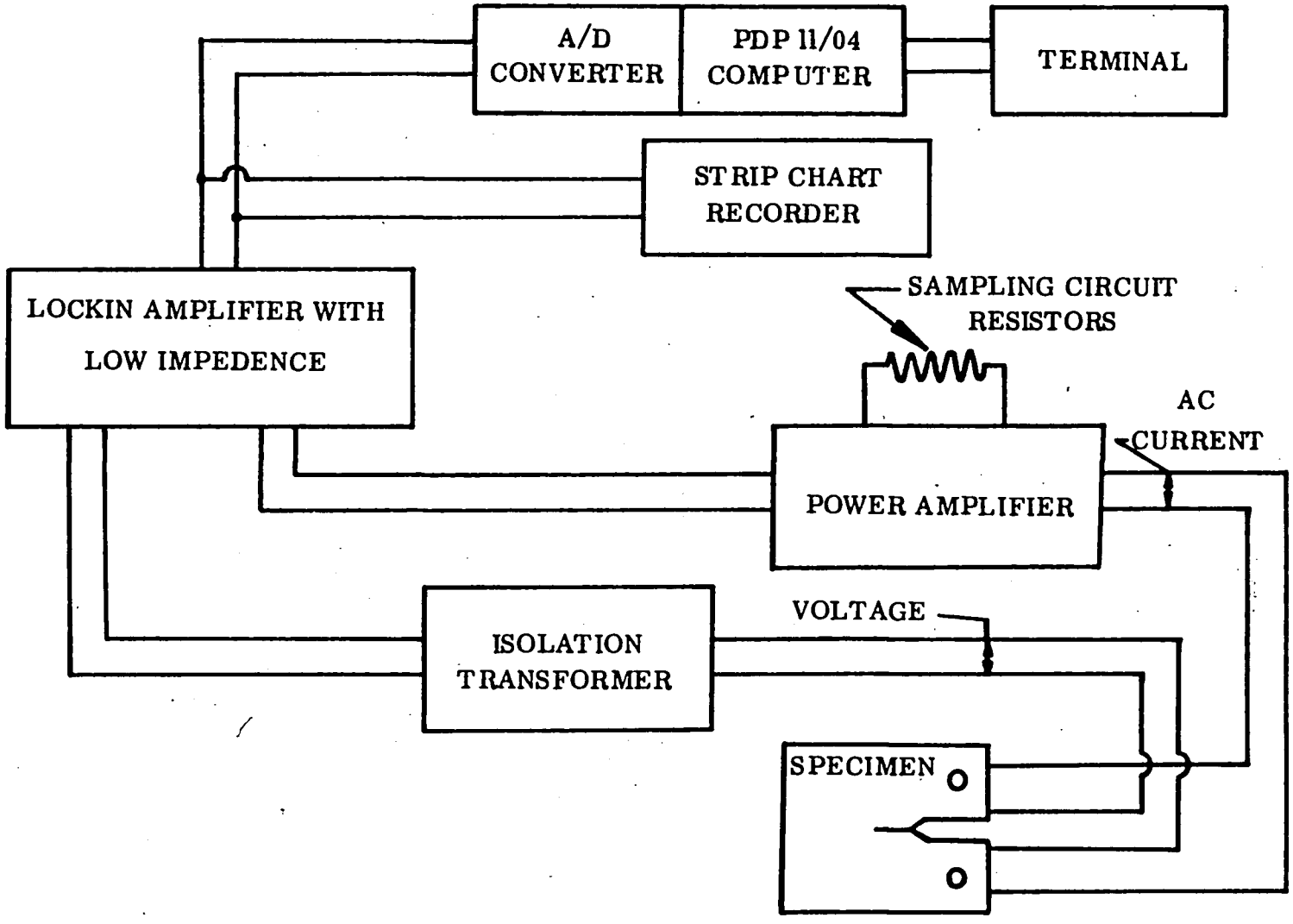

Fig. 6. Schematic of electrical potential crack measurement system.

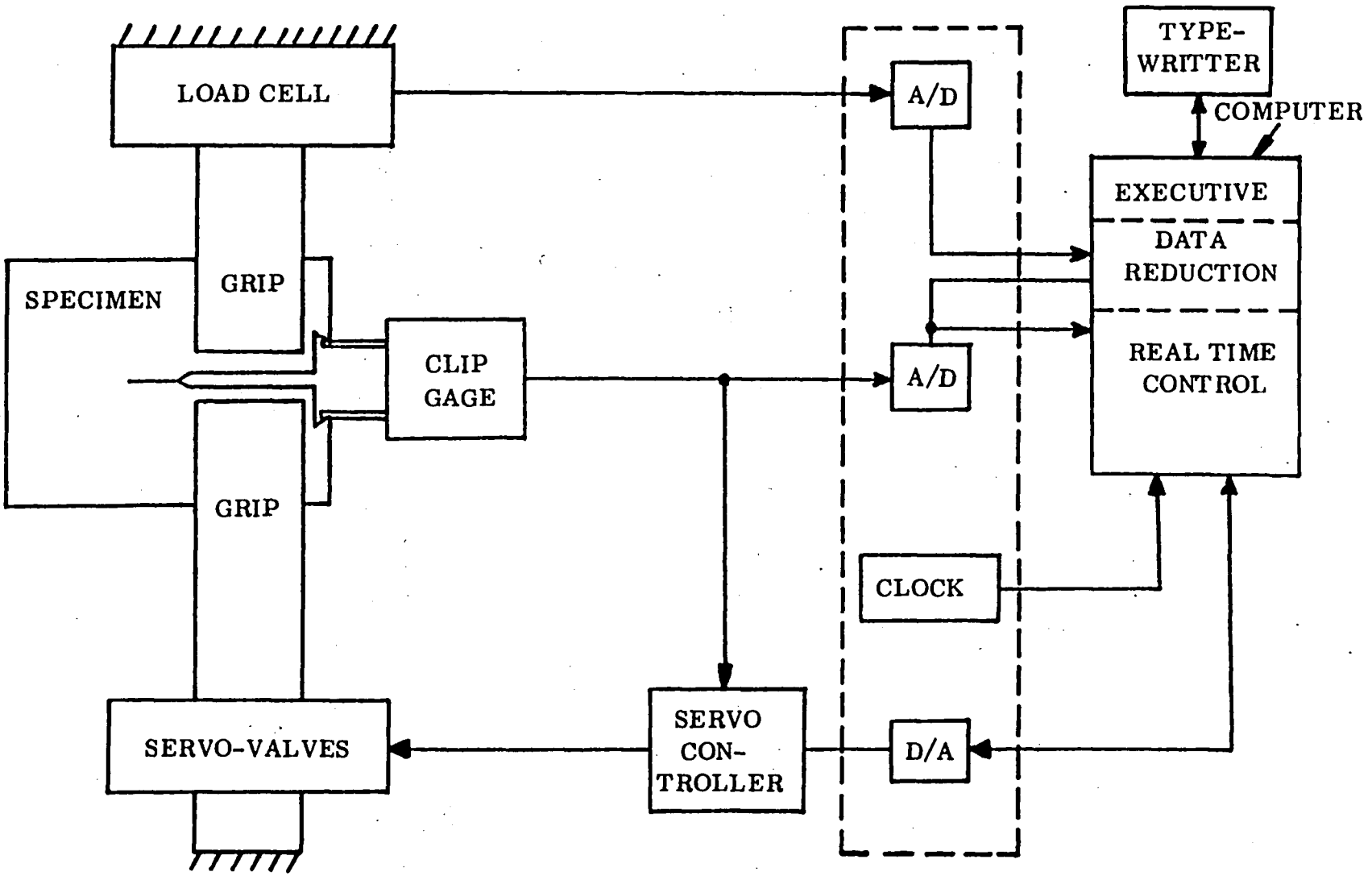

Fig. 7. Schematic of constant displacement crack measurement system.

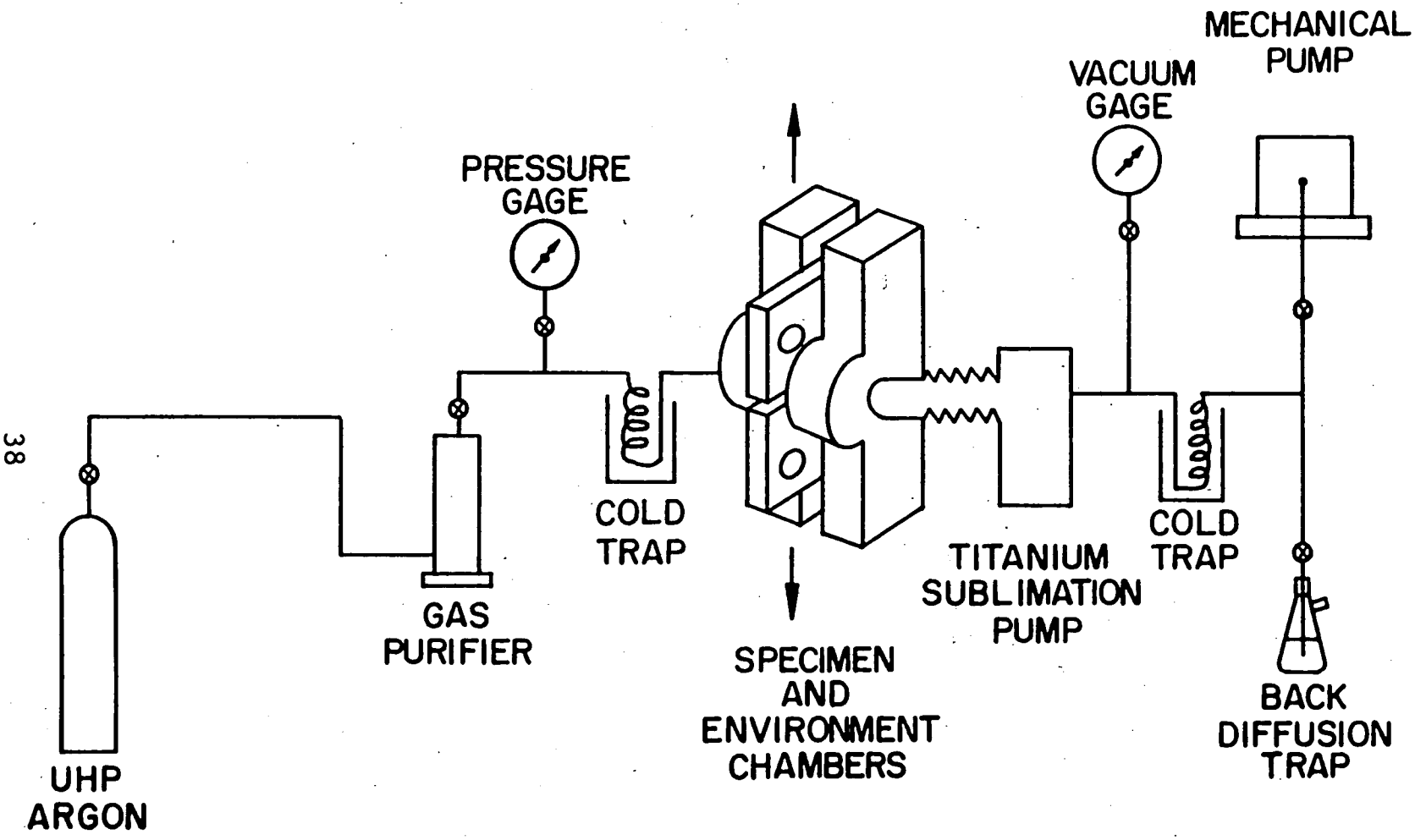

Fig. 8. Schematic diagram of the environment control system.

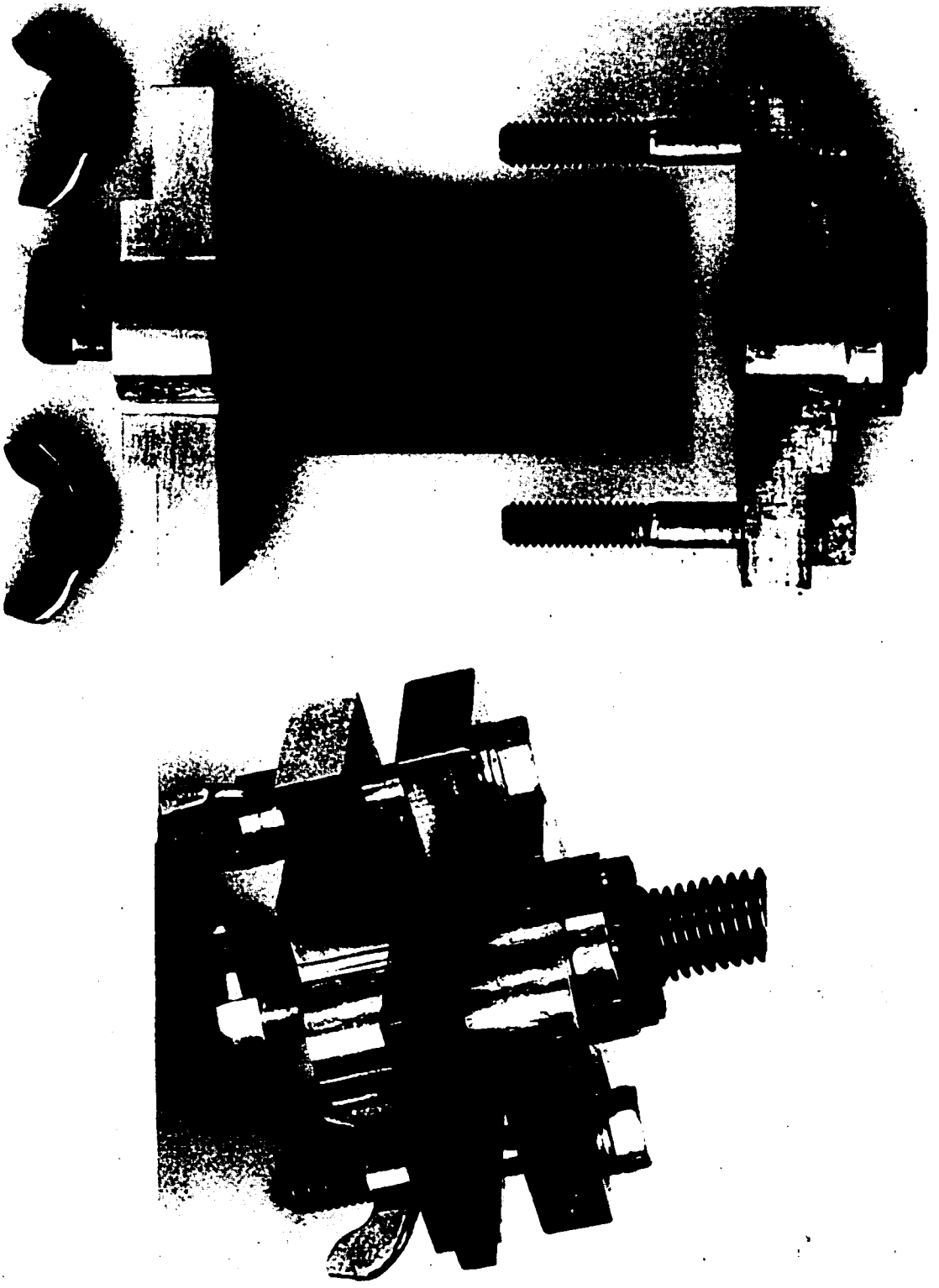

Fig. 9. Photograph of WOL specimen and environment chamber

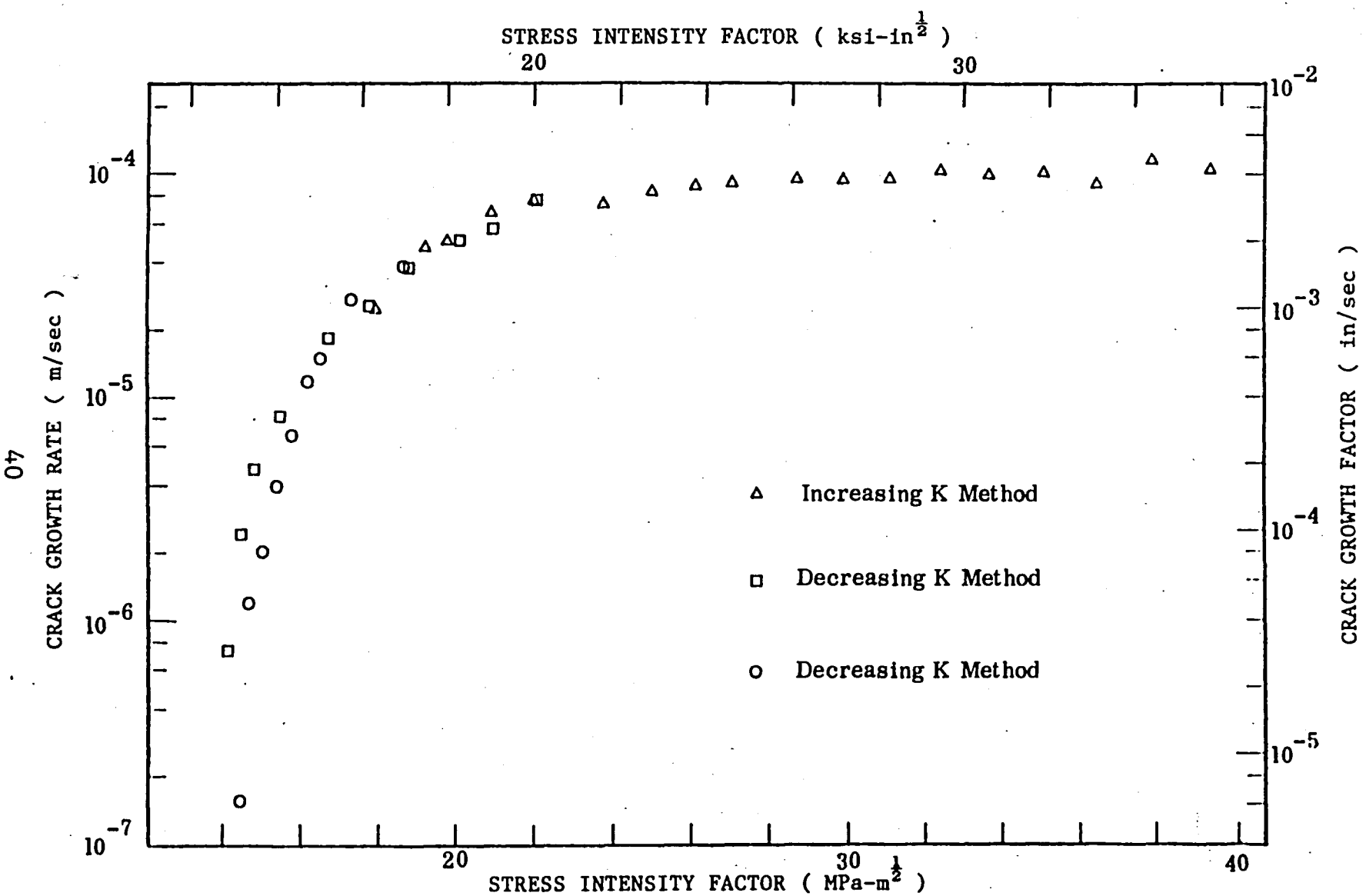

Fig. 10. Kinetics of hydrogen enhanced crack growth at room temperature in normal purity AISI 4340 steel.

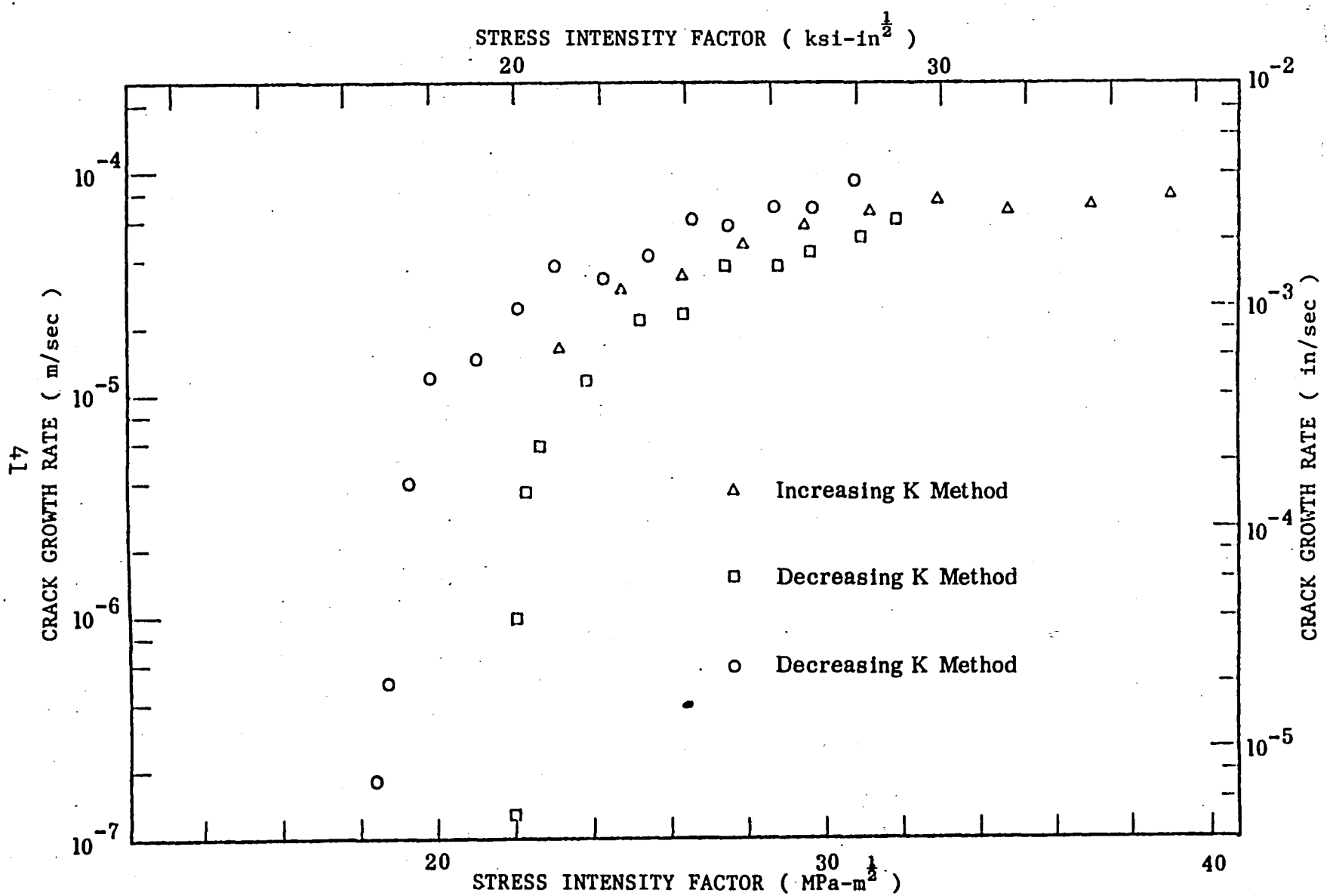

Fig. 11. Kinetics of hydrogen enhanced crack growth at room temperature in high purity AISI 4340 steel.

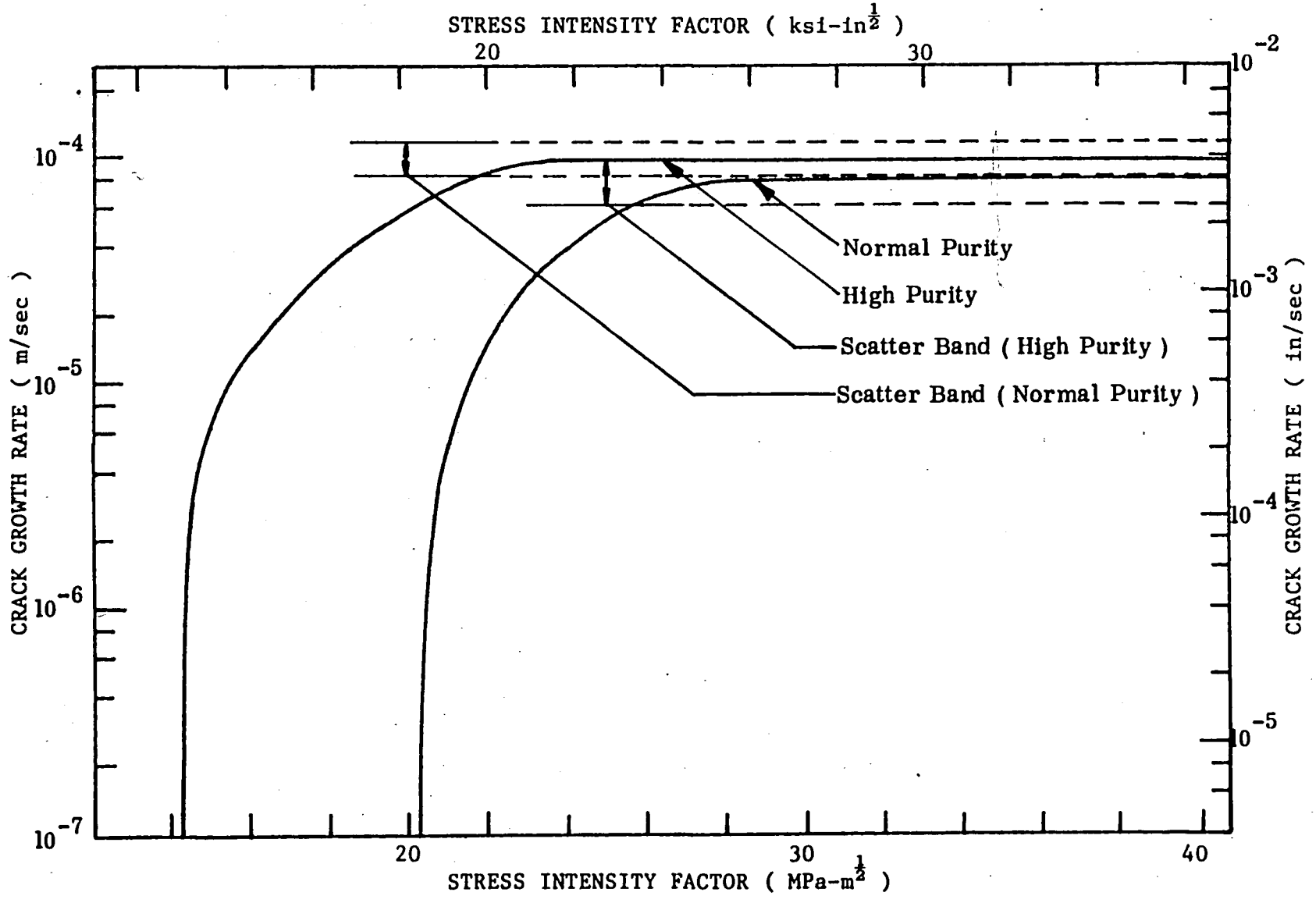

Fig. 12. Comparison of crack growth rate of normal and high purity AISI 4340 steel.

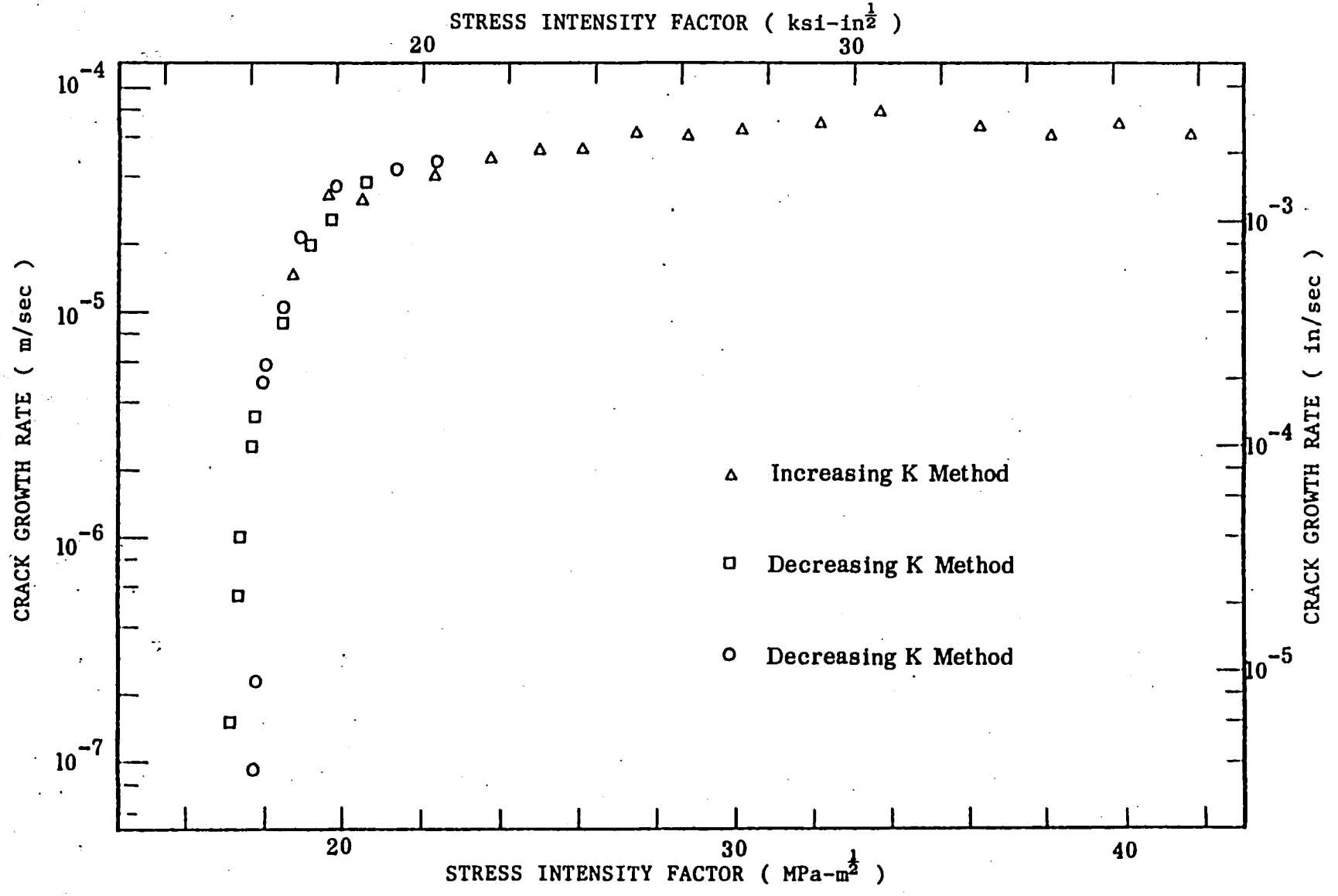

Fig. 13. Kinetics of hydrogen enhanced crack growth at room temperature in normal purity 18Ni maraging steel.

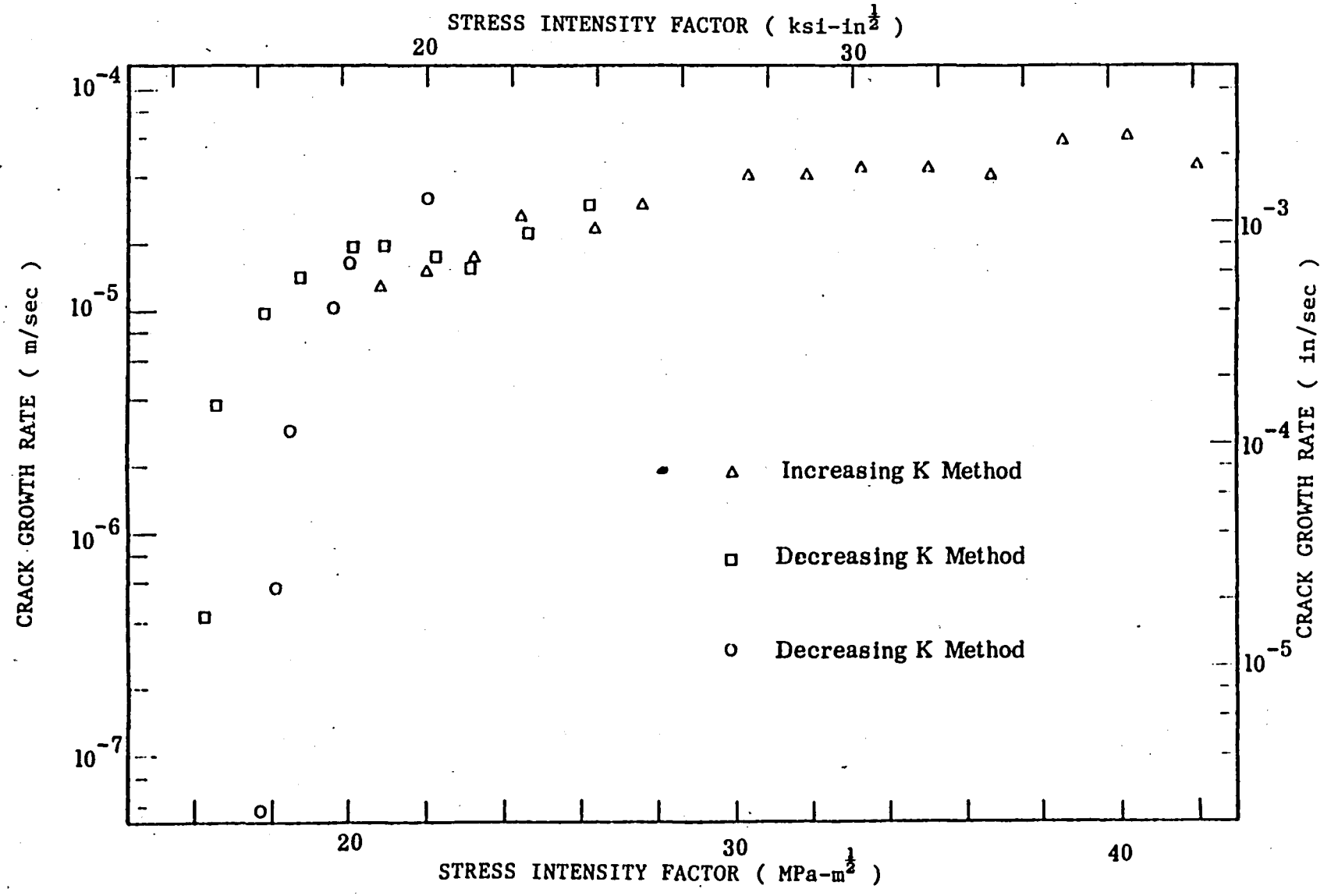

Fig. 14. Kinetics of hydrogen enhanced crack growth at room temperature in high purity 18Ni maraging steel.

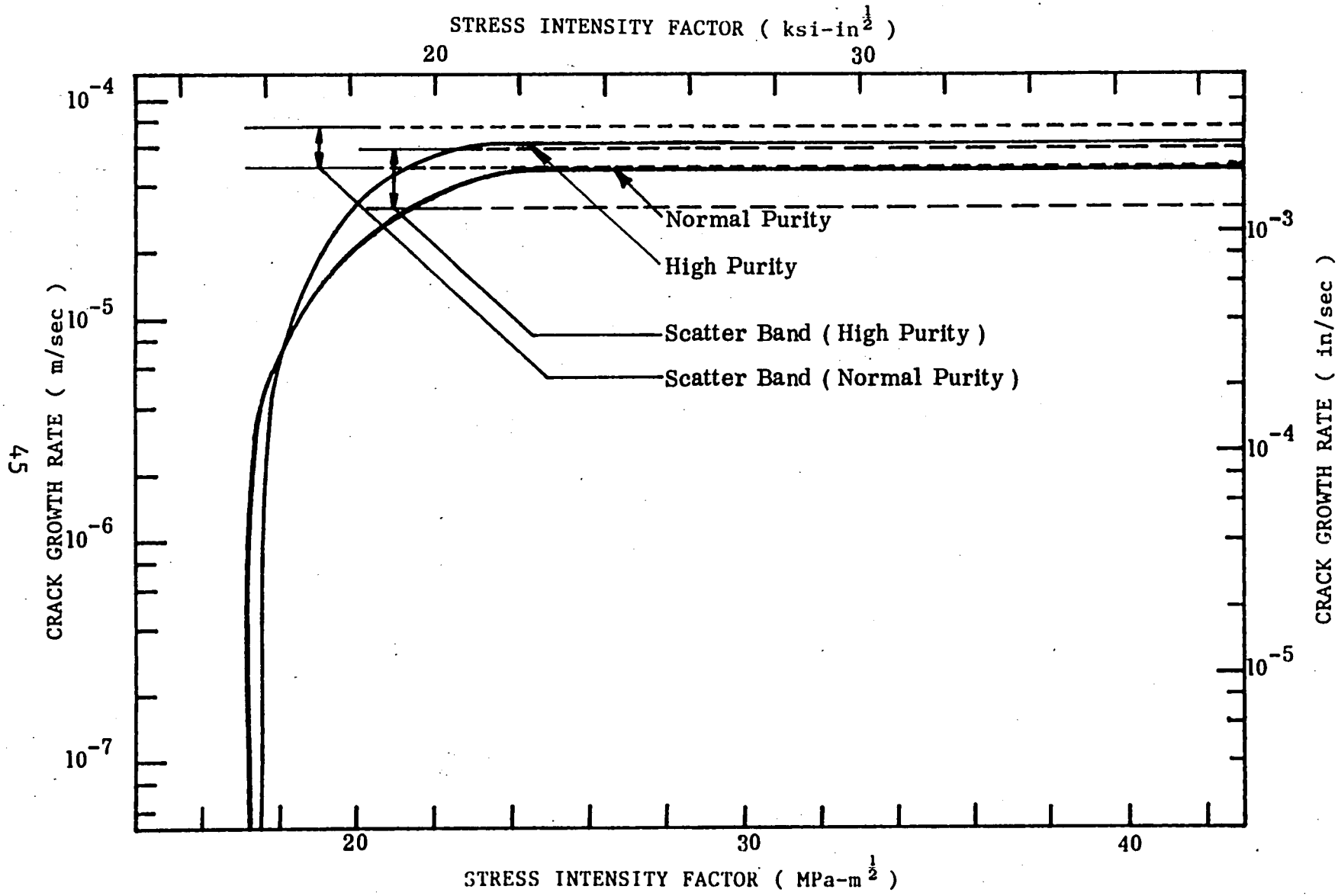

Fig. 15. Comparison of crack growth rate of normal and high purity 18Ni maraging steel.

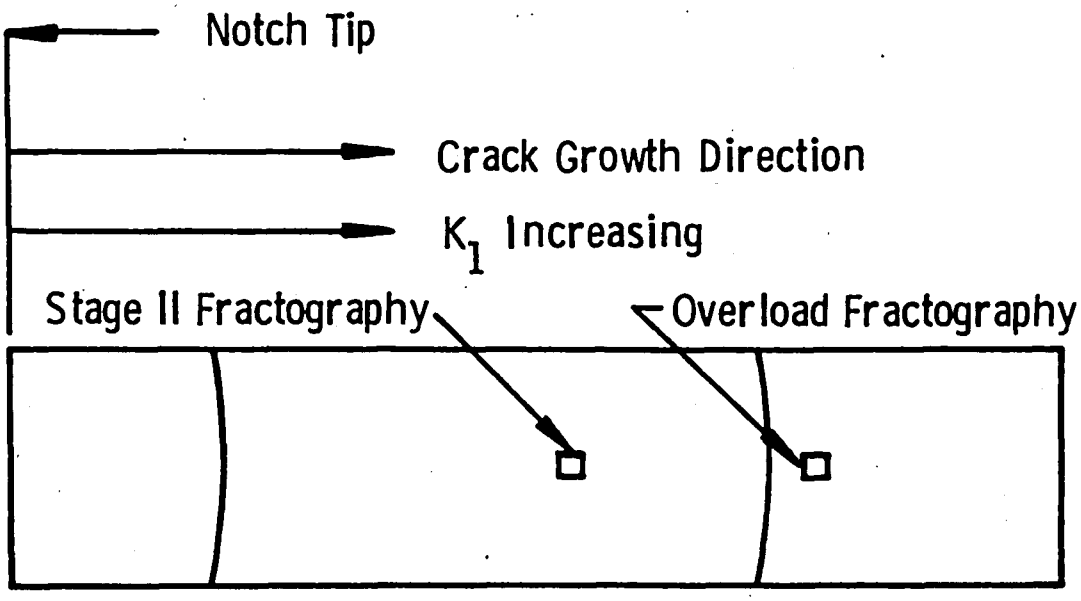

(a)

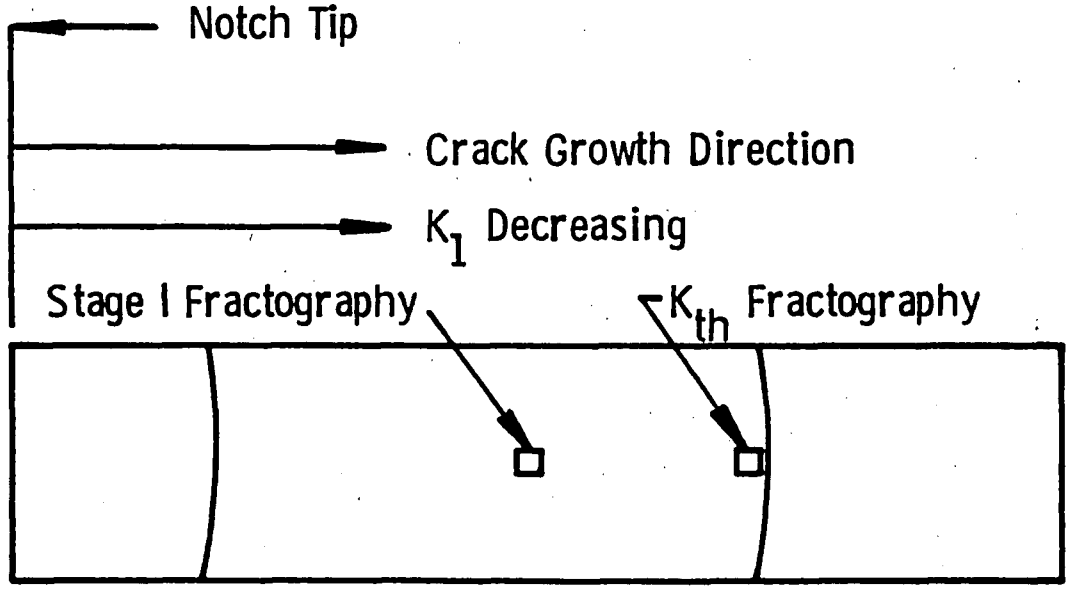

(b)

Fig. 16. Schematic diagram of fracture surface showing the location of SEM fractographs: (a) Increasing K test; (b) Decreasing K test.

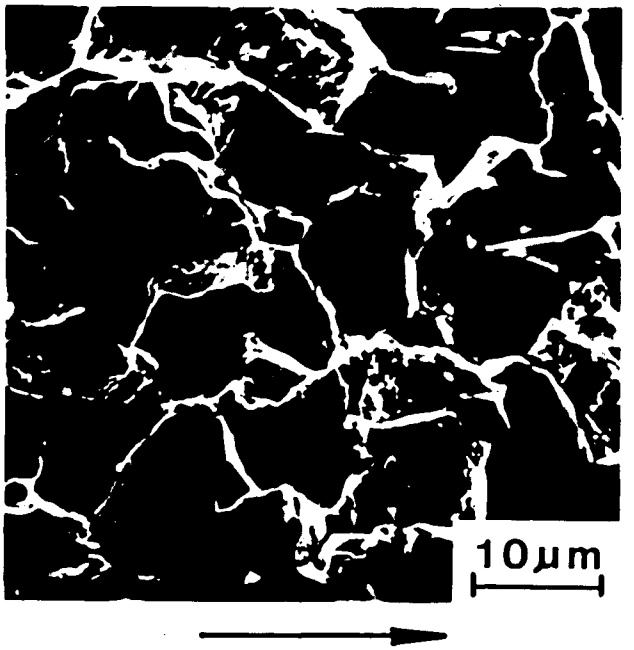

Fig. 17. A comparison between fracture surface morphologies characteristic of hydrogen assisted crack growth in normal purity and high purity AISI 4340 steels near K threshold. (P_{H_2} =133 kPa and R.T.) (a) normal purity K=14.2 MPa-$m^{\frac{1}{2}}$, (b) high purity, K=20.4 MPa-$m^{\frac{1}{2}}$.

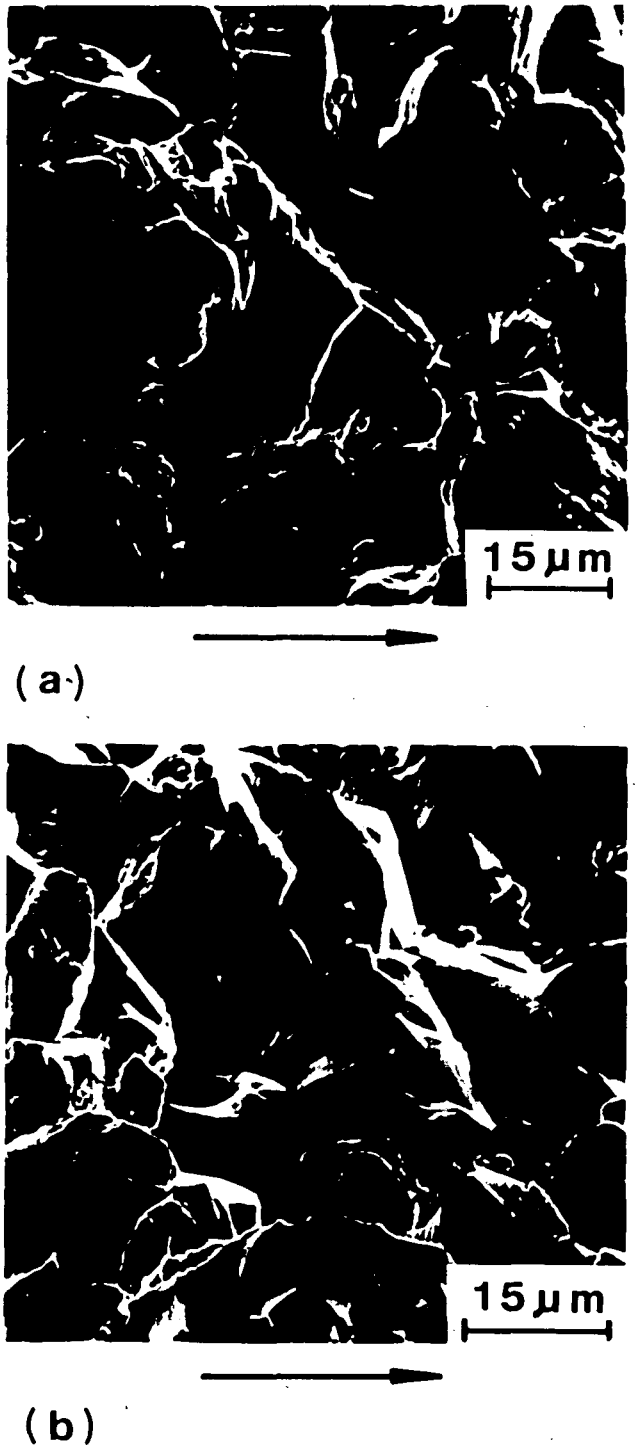

Fig. 18. A comparison between fracture surface morphologies characteristic of hydrogen assisted crack growth in normal purity and high purity 18Ni maraging steels near K threshold (P_{H_2} =133 kPa and R.T.) (a) normal purity, K = 17.6 MPa-$m^{1/2}$ (b) high purity, K = 17.1 MPa-$m^{1/2}$.

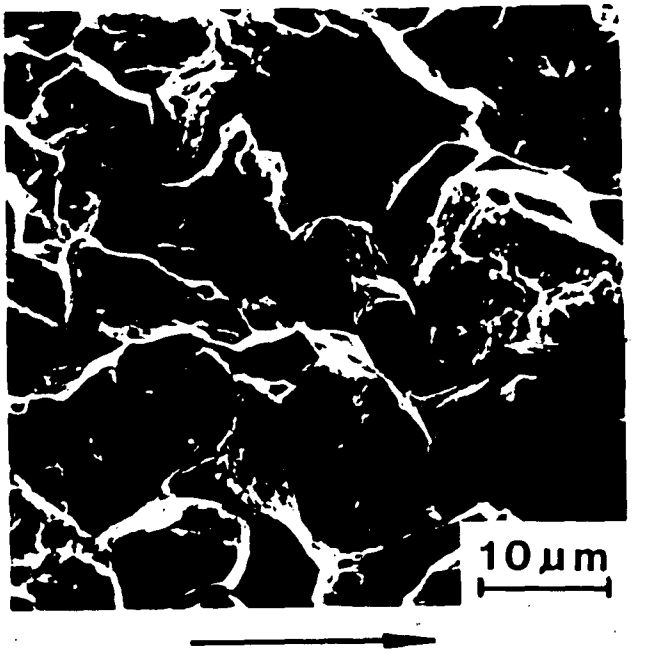

(a)

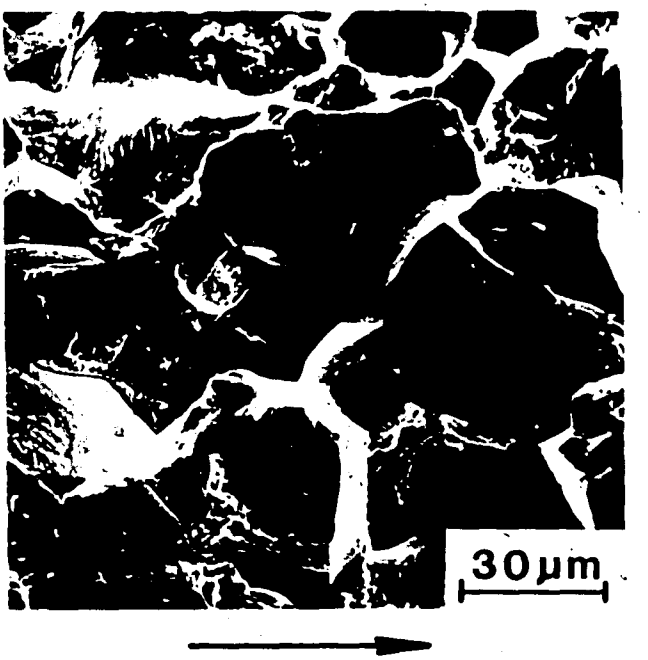

(b)

Fig. 19. A comparison between fracture surface morphologies characteristic of hydrogen assisted crack growth in normal purity and high purity AISI 4340 steels at Stage I. (P_{H_2} =133 kPa and R.T.) (a) normal purity, K=15.6 MPa-$m^{1/2}$, (b) high purity, K=20.9 MPa-$m^{1/2}$.

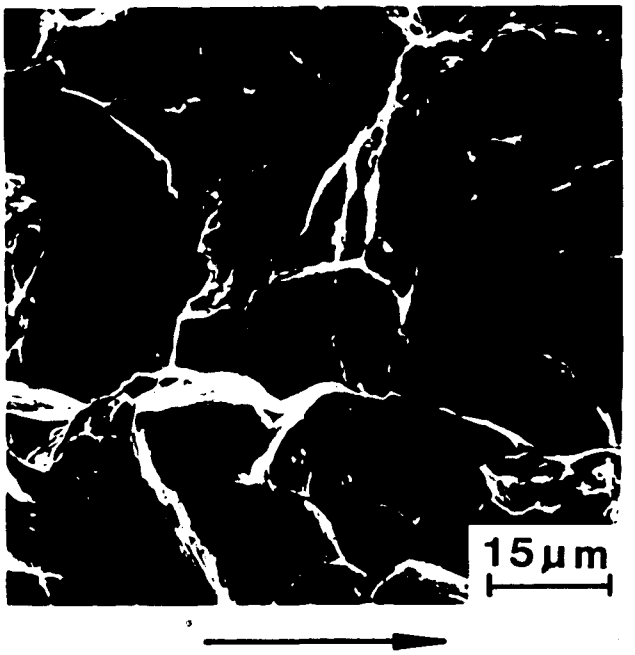

(a)

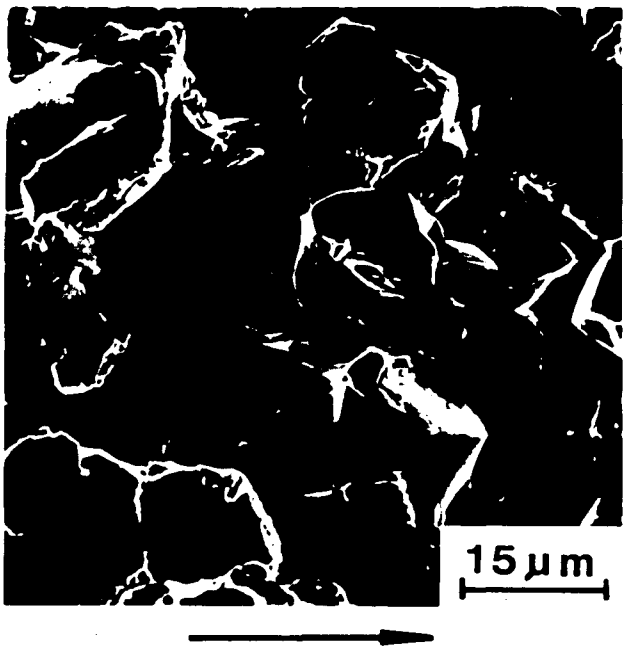

(b)

Fig. 20. A comparison between fracture surface morphologies characteristic of hydrogen assisted cracking growth in normal purity and high purity 18Ni maraging steels at Stage I. (P_{H_2} =133 kPa and R.T.) (a) normal purity, K=18.7 MPa-$m^{1/2}$, (b) high purity, K=18.7 MPa-$m^{1/2}$.

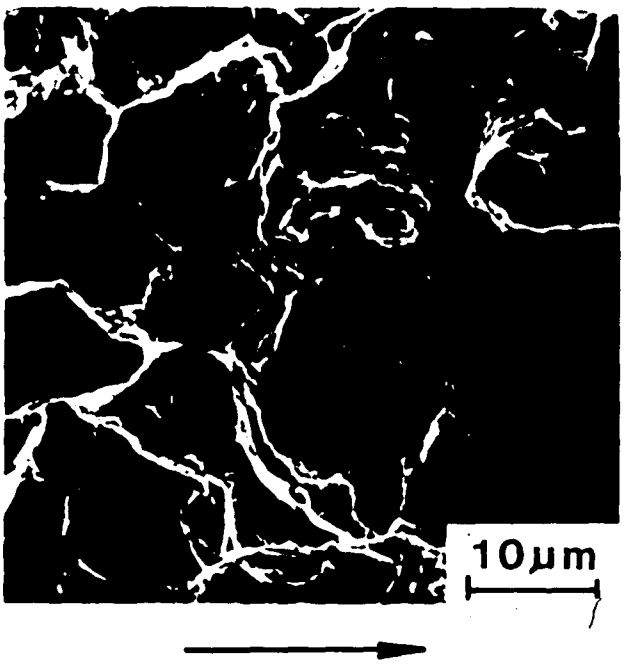

(a)

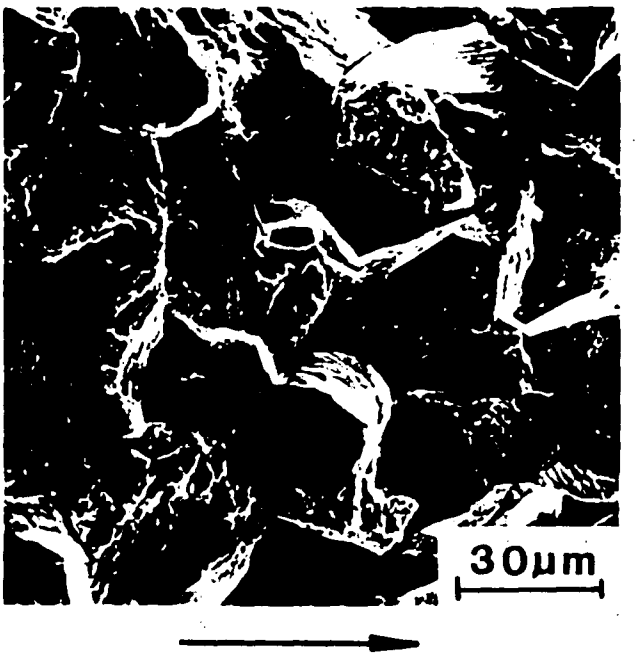

(b)

Fig. 21. A comparison between fracture surface morphologies characteristic of hydrogen assisted crack growth in normal purity and high purity AISI 4340 steels at Stage II. (P_{H_2} =1.33 kPa and R.T.) (a) normal purity, K=33 MPa-$m^{1/2}$, (b) high purity, K=33 MPa-$m^{1/2}$

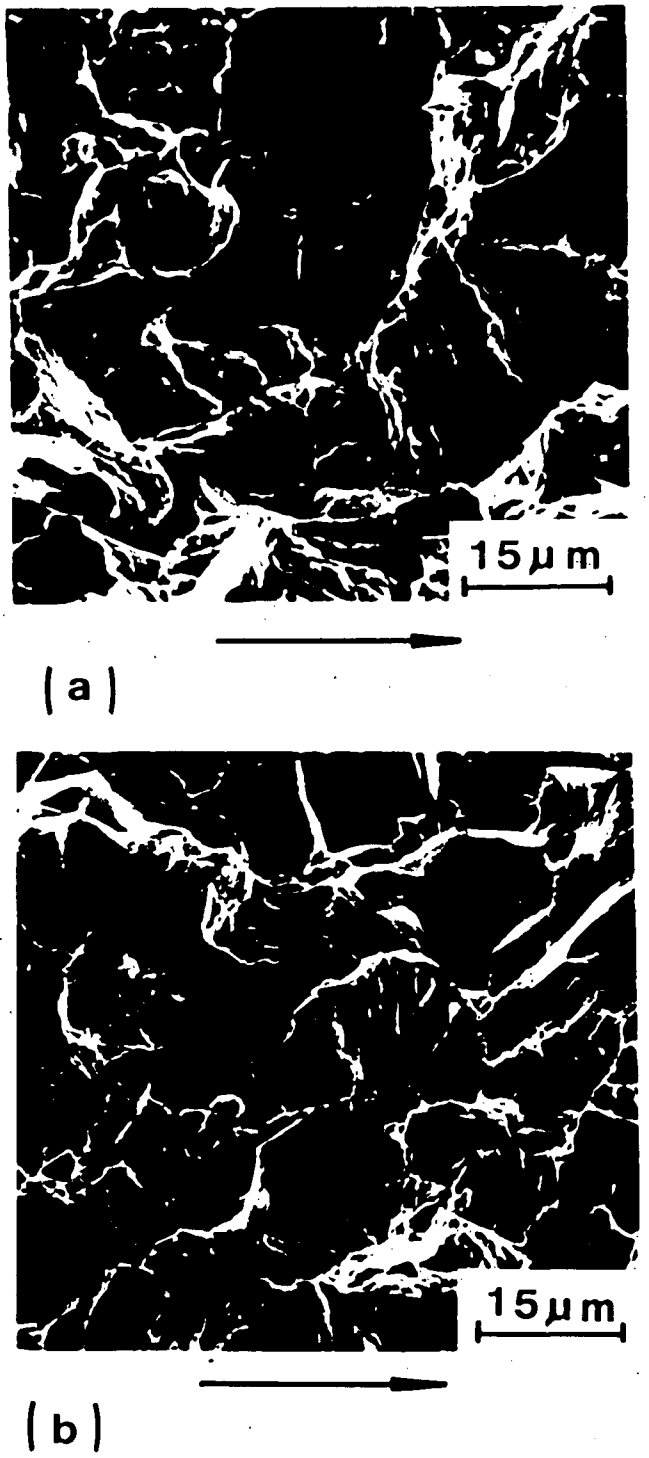

Fig. 22. A comparison between fracture surface morphologies characteristic of hydrogen assisted crack growth in normal purity and high purity 18Ni maraging steels at Stage II. (P_{H_2}=133 kPa and R.T.) (a) normal purity, K=31.9 MPa-$m^{\frac{1}{2}}$, (b) high purity, K=31.9 MPa-$m^{\frac{1}{2}}$.

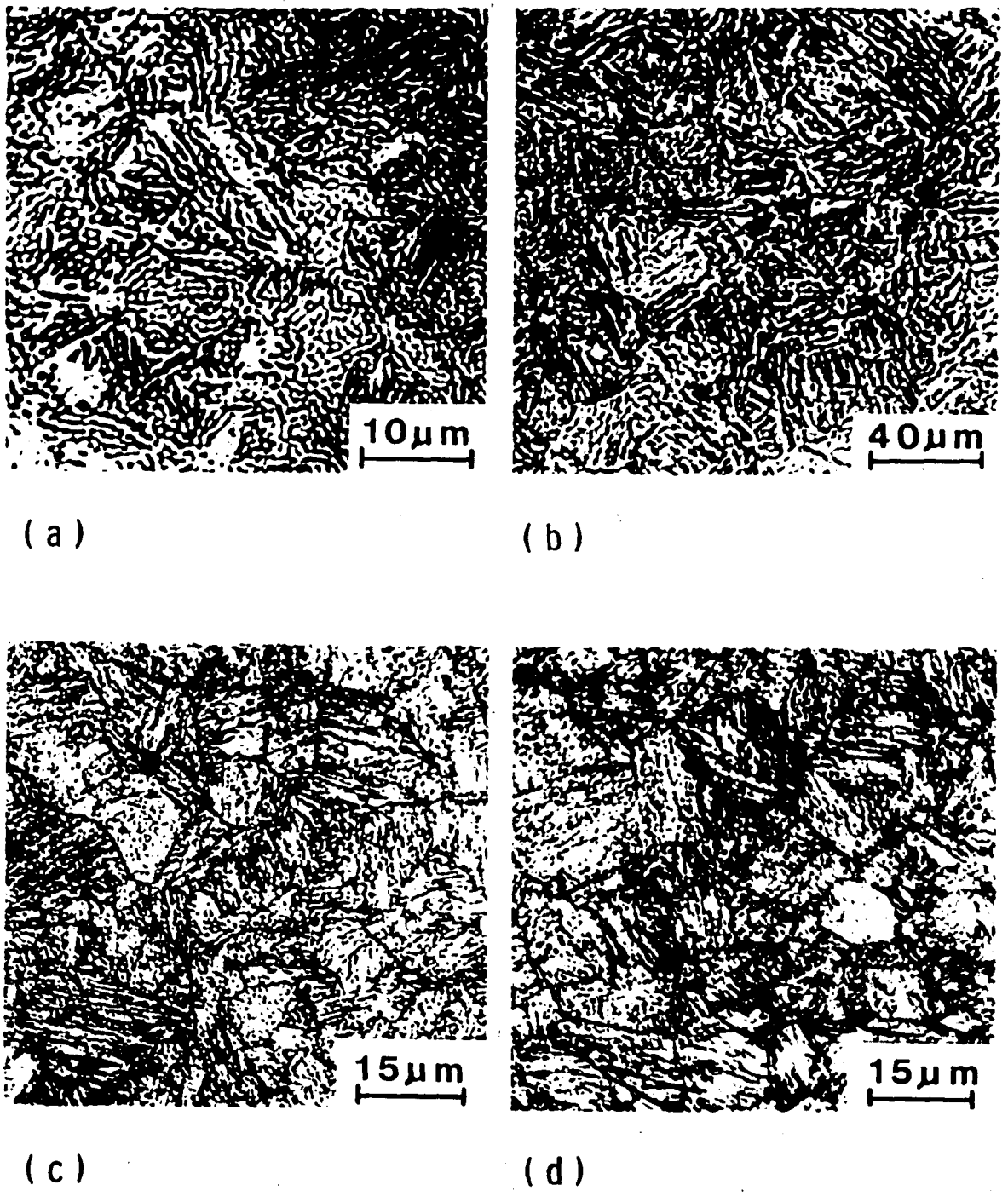

Fig. 23. Microstructure of AISI 4340 steel and 18Ni maraging steel. (a) normal purity AISI 4340 steel, (b) high purity AISI 4340 steel, (c) normal purity 18Ni maraging steel, (d) high purity 18Ni maraging steel.

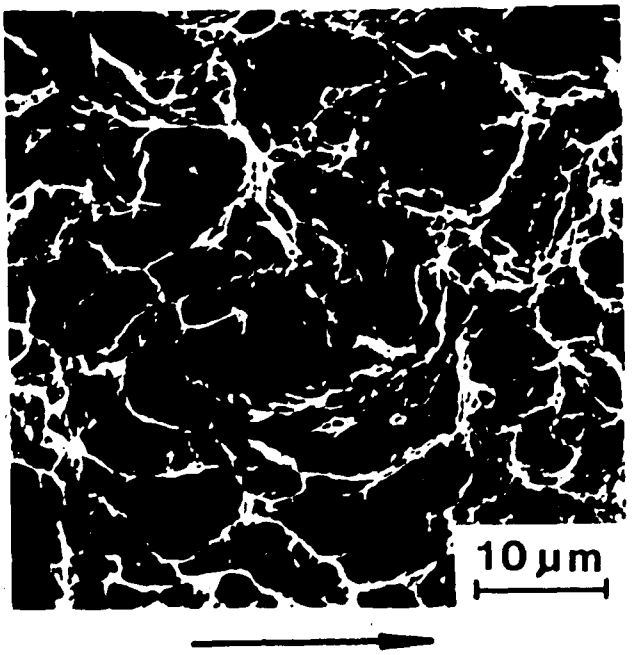

(a)

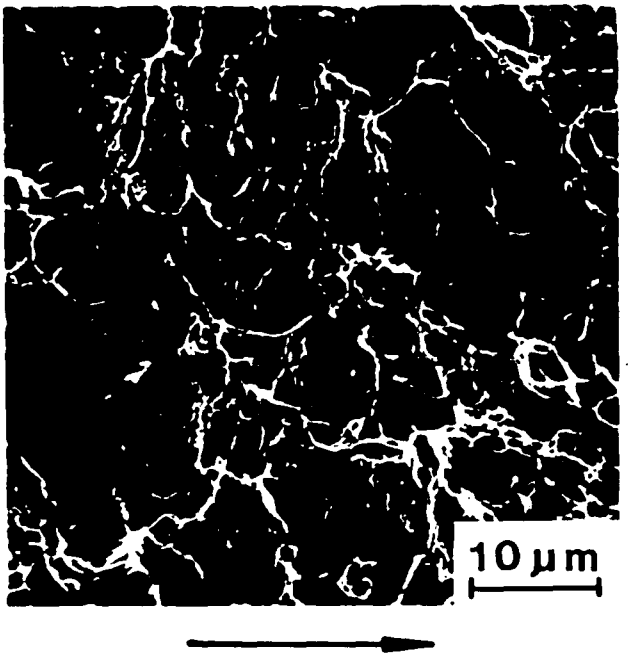

(b)

Fig. 24. A comparison between fracture surface morphologies of normal purity and high purity AISI 4340 steels broken by tensile overload in air at room temperature. (a) normal purity, (b) high purity.

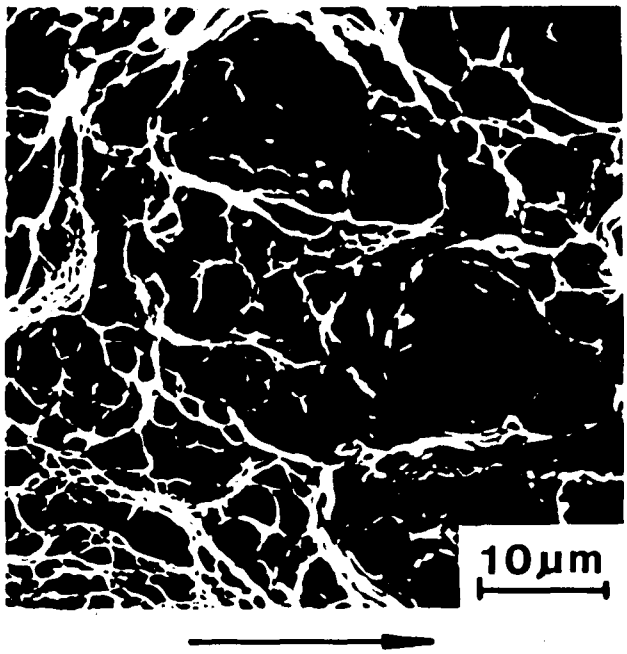

(a)

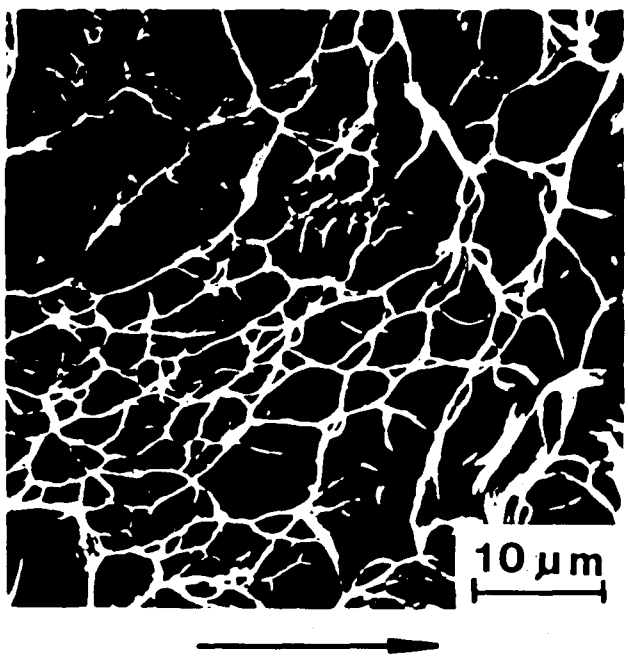

(b)

Fig. 25. A comparison between fracture surface morphologies of normal purity and high purity 18Ni maraging steel broken by tensile overload in air at room temperature. (a) normal purity, (b) high purity.

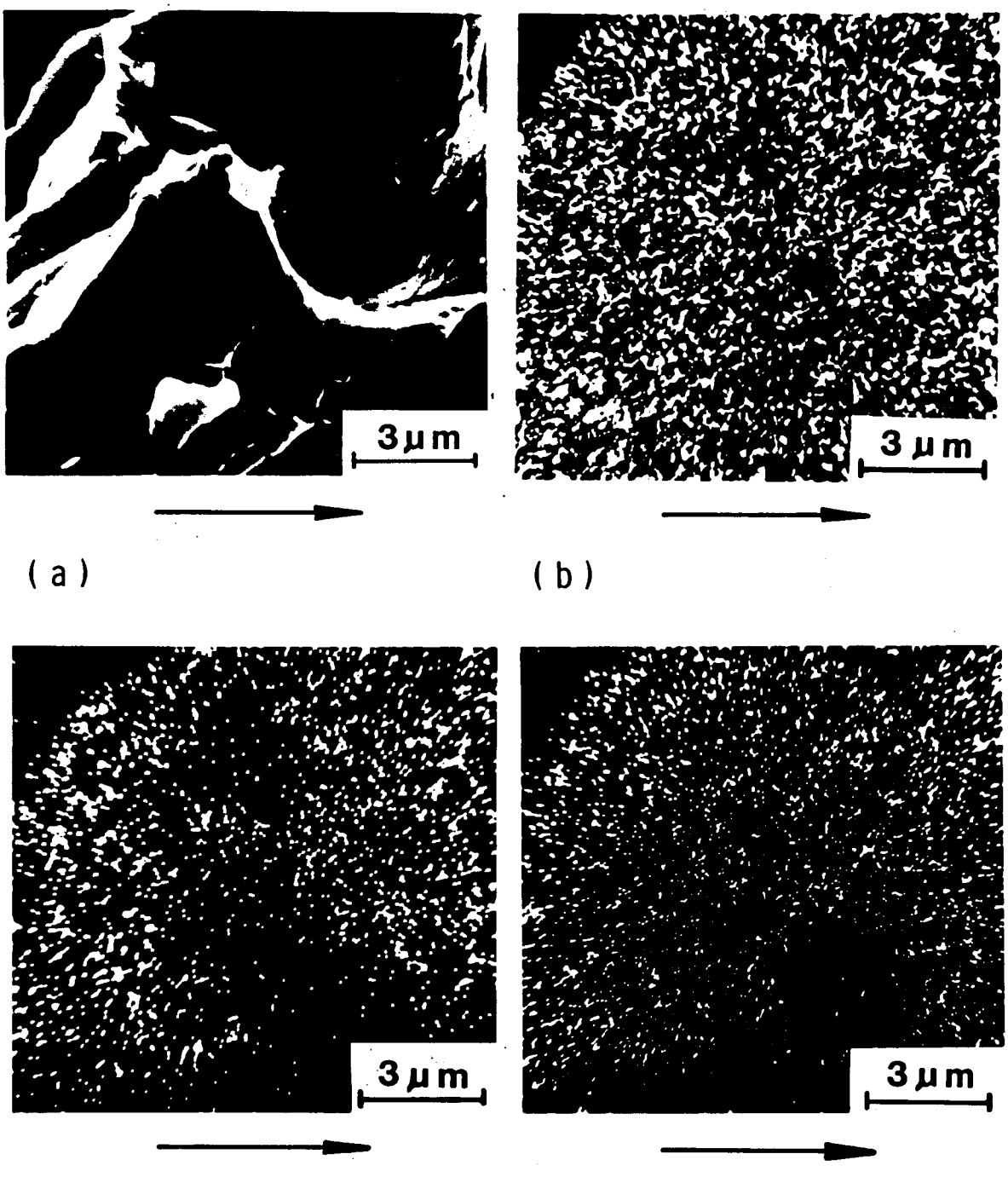

Fig. 26. SEM micrograph and X-ray microscan images of inclusions on grain boundary of normal purity 18Ni maraging steel tested in hydrogen. (a) SEM micrograph of inclusion on grain boundary, (b) X-ray scan image - Fe radiation, (c) X-ray scan image - Ni radiation, (d) X-ray scan image - S radiation.

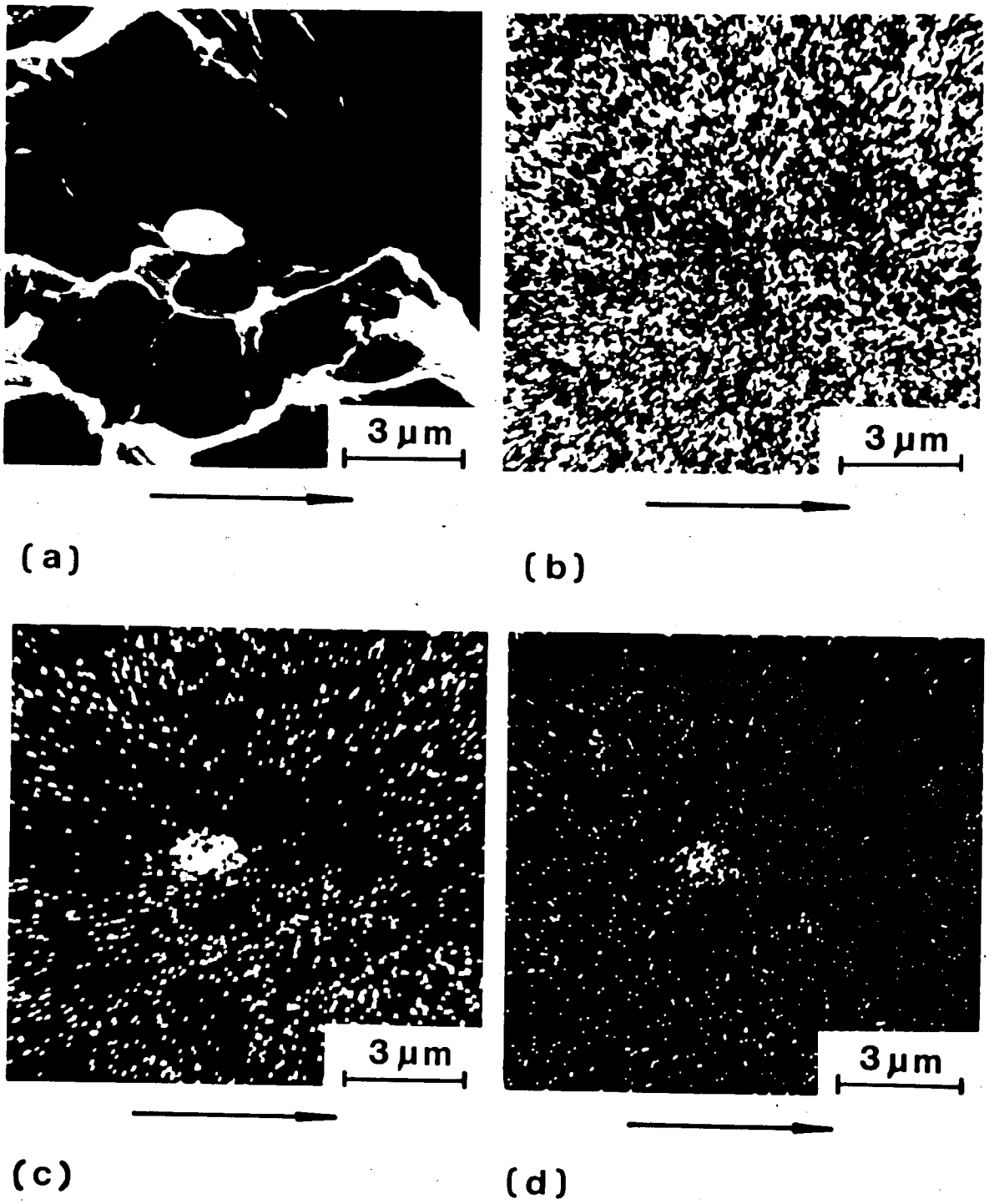

Fig. 27. SEM micrograph and X-ray microscan images of manganese sulfide (MnS) inclusion on grain boundary of normal purity AISI 4340 steel tested in hydrogen. (a) SEM micrograph of inclusion on grain boundary, (b) X-ray scan image - Fe radiation, (c) X-ray scan image - S radiation, (d) X-ray scan image - Mn radiation.

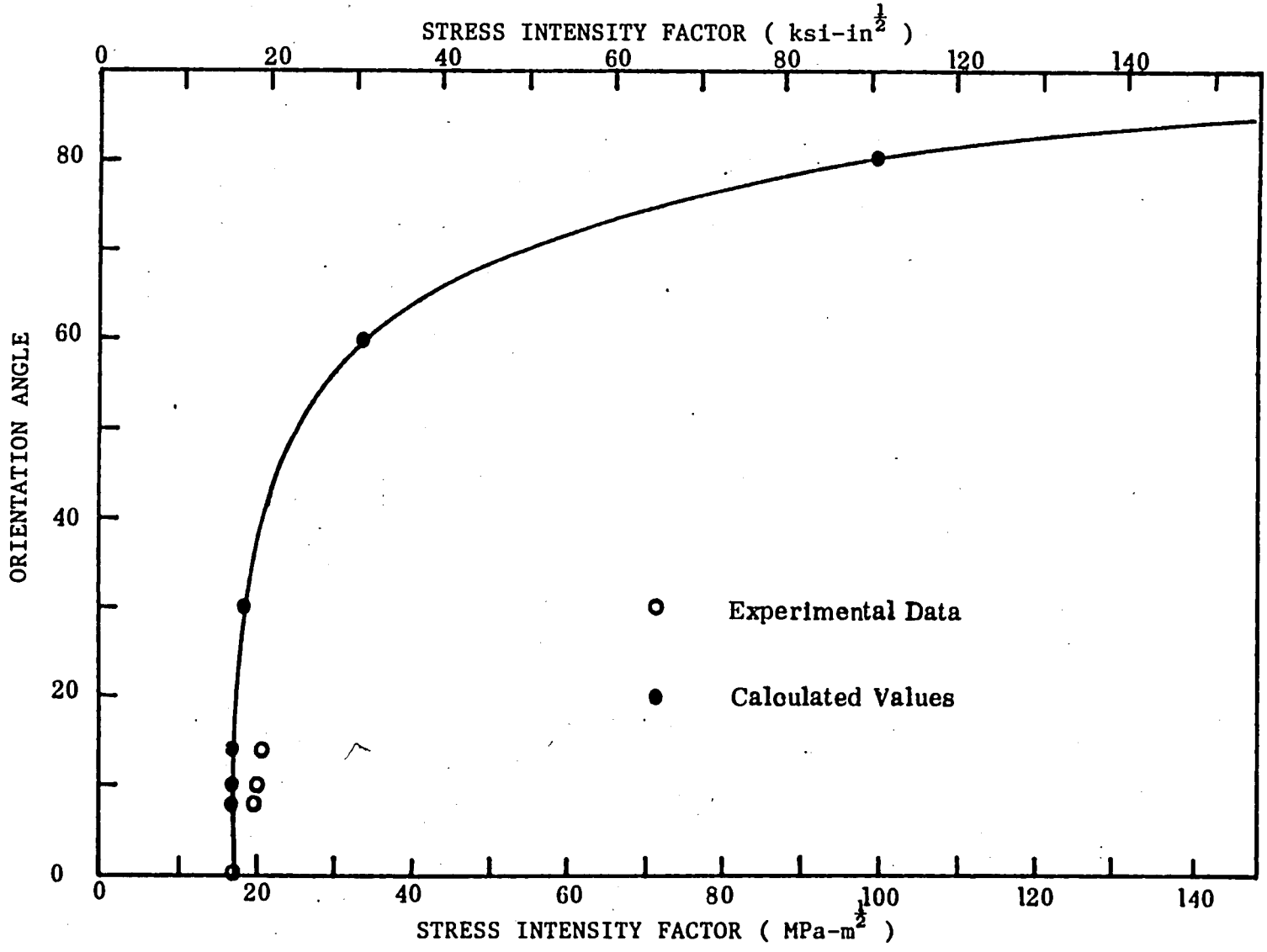

Fig. 28. Influence of crack orientation on K threshold (K_{th}) values. K_{th} is taken to be 17.6 MPa-$m^{1/2}$ at 0°.

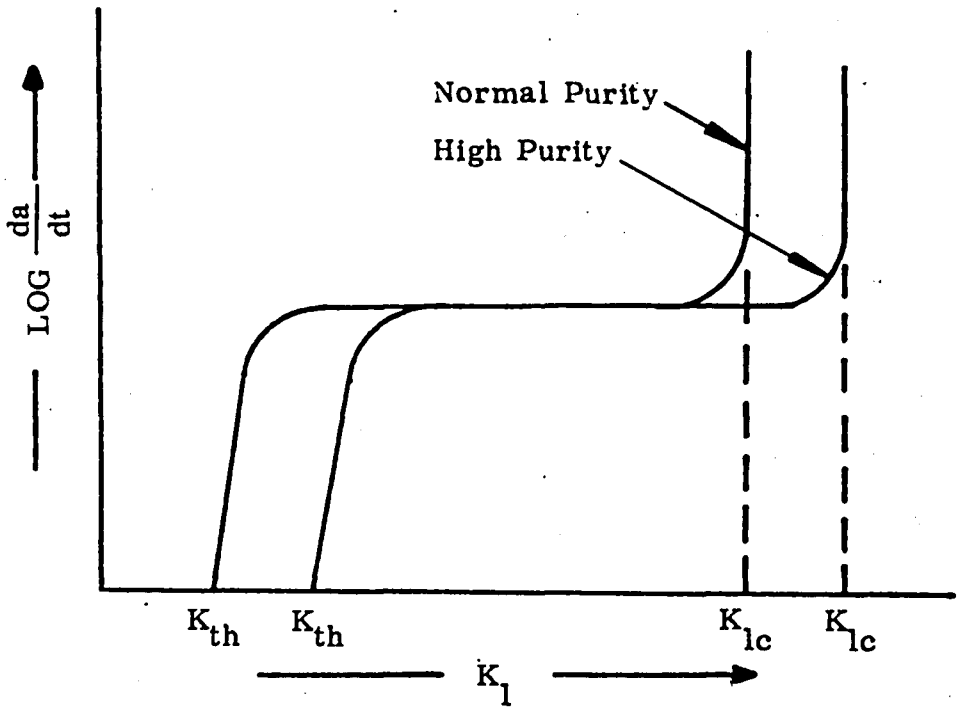

Fig. 29. Schematic of crack growth kinetics for normal purity and high purity AISI 4340 steel.

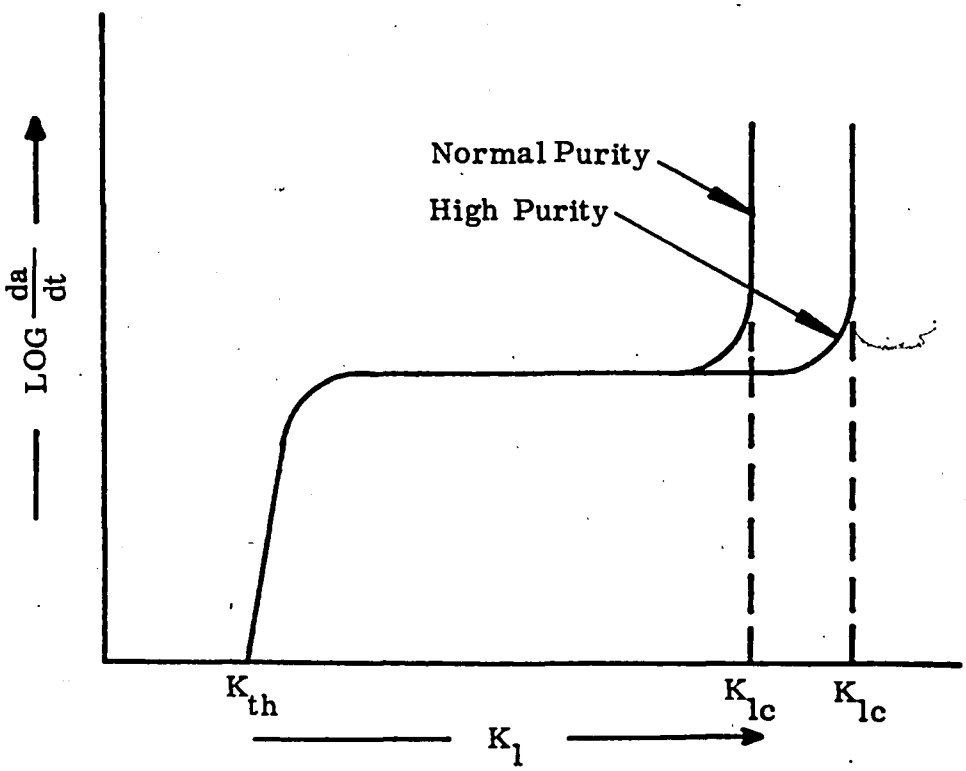

Fig. 30. Schematic of crack growth kinetics for normal purity and high purity 18Ni maraging steel.

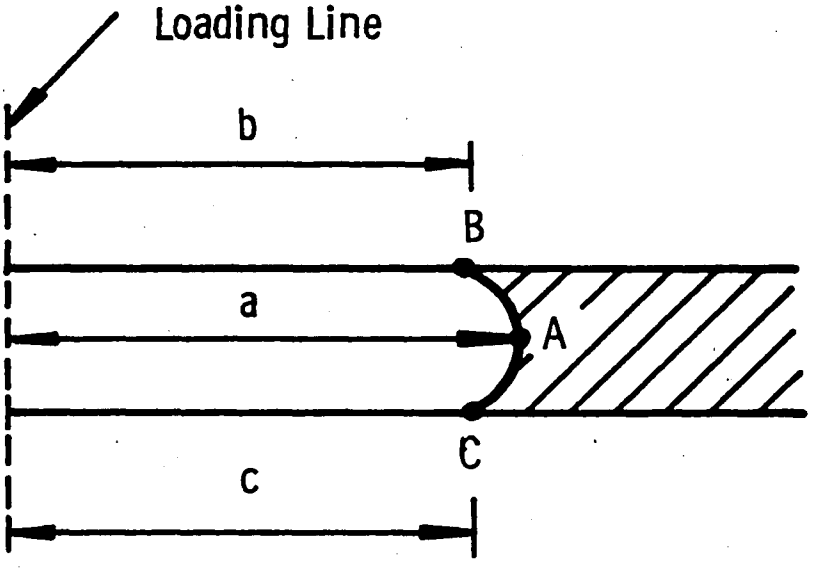

Fig. A1. Crack front geometry and related parameters.

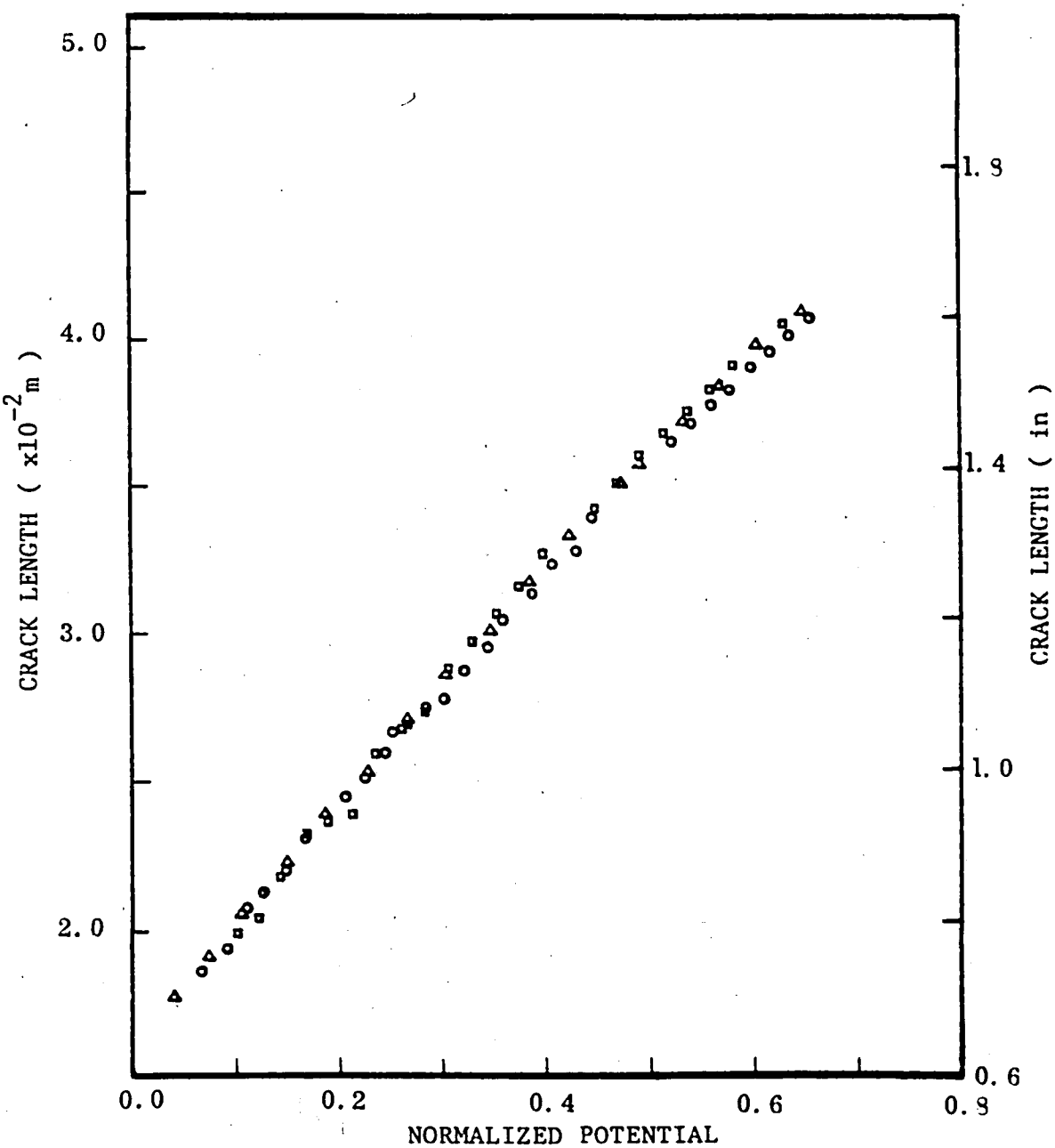

Fig. A2. Electrical potential versus visual measurements of crack lengths.

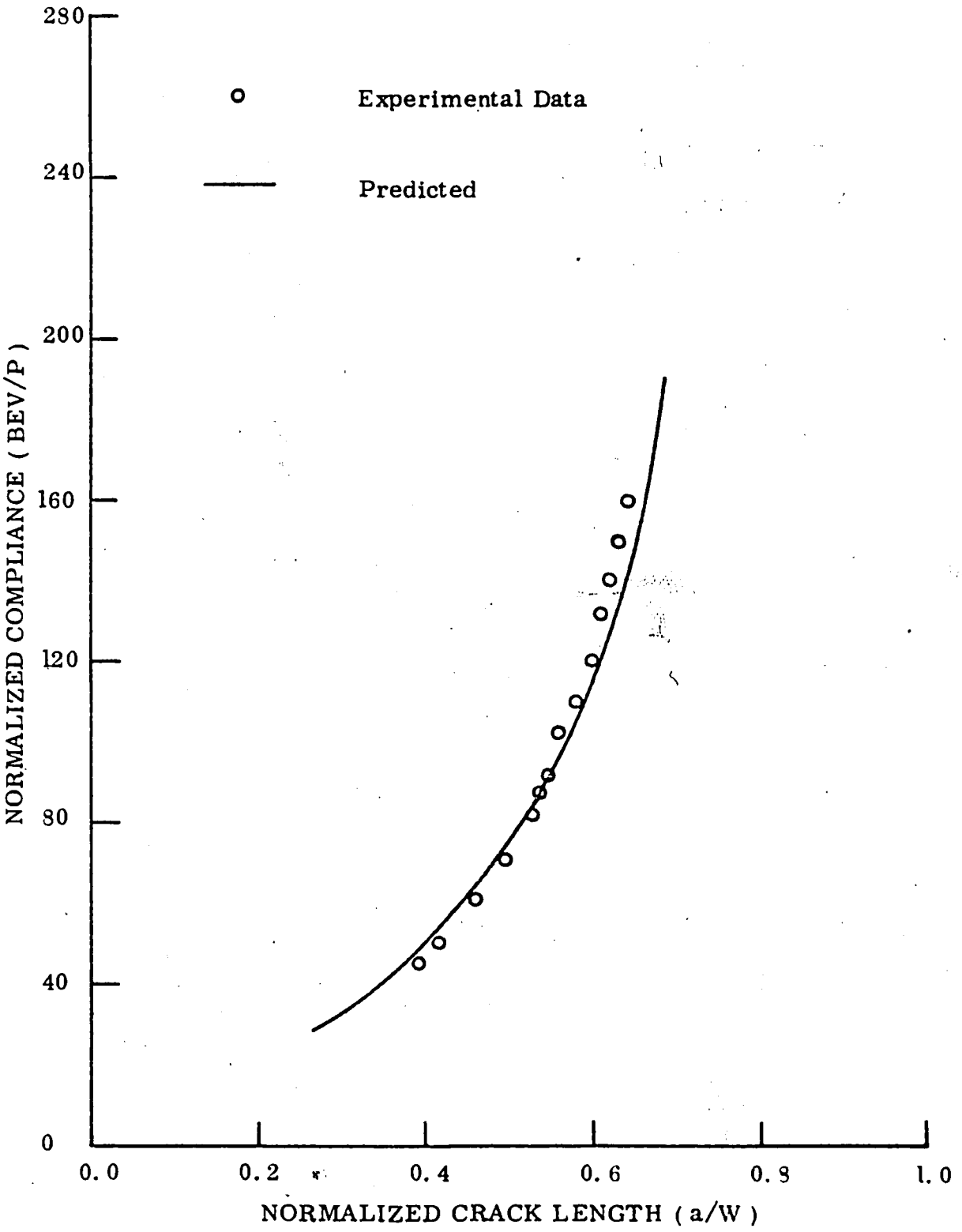

Fig. A3. Comparison of predicted compliances with experimental data for WOL specimen.

TABLE I

Chemical Composition of Normal-and High-Purity Steels - Weight Percent [9]

Steel	C	Mn	P	S	Si	Ni	Cr	Mo	Co
4340 N.P.	0.40	0.71	0.010	0.011	0.27	1.80	0.82	0.25	0.008
4340 H.P.	0.40	0.29	<0.0003	0.0008	0.007	1.79	0.75	0.27	0.023
18Ni N.P.	0.032	0.11	0.011	0.009	0.10	18.00	<0.05**	4.82	7.71
18Ni H.P.	<0.005	0.001	0.0006	0.0005	0.011	18.22	<0.005	4.81	7.75

Steel	O	Al*	N	Ti	As	Sb	Sn	Cu
4340 N.P.	0.0016	0.034	0.008	0.005	<0.002	<0.0004	<0.002	0.006
4340 H.P.	0.0010	0.002	0.0020	<0.002	<0.002	<0.0004	<0.002	0.002
18Ni N.P.	0.0017	0.019	0.008	0.43	<0.002	<0.0004	<0.002	0.004
18Ni H.P.	0.0014	0.013	0.0016	0.43	<0.002	<0.0004	<0.002	0.004

* Total aluminum content.

** Detection limit for X-ray analysis technique employed.

Table II

Heat Treatment

Steel	Treatment
4340 N. P. 4340 H. P.	1 HR 900°C, OQ + 1 HR 830°C, OQ + 8 HRS 250°C, AC
18Ni N. P. 18Ni H. P.	1 HR 900°C, WQ + 1 HR, 830°C WQ + 5 HRS 480°C, WQ

AC = Air Cool

OQ = Oil Quench

WQ = Water Quench

Table III

Mechanical Properties of Steels

Steel	Yield Strength (0.2% Offset) Mpa (ksi)	Tensile Strength Mpa (ksi)	Elongation in 1 Inch %	Reduction of Area %	Charpy V-notch Energy Absorbed ft-lb (RT)	Youngs' Modulus Mpa (ksi)
4340 N. P.	1510 (219)	1786 (259)	11.6	43.3	12	19.9×10^7 (2.9×10^7)
4340 H. P.	1448 (210)	1703 (247)	11.6	45.4	14	19.9×10^7 (2.9×10^7)
18Ni N. P.	1654 (240)	1738 (252)	10.0	44.2	14	18.6×10^7 (2.7×10^7)
18Ni H. P.	1675 (243)	1758 (255)	13.0	65.7	50	18.6×10^7 (2.7×10^7)

RT = Room Temperature

Table IV

Prior Austenite Grain Size

Specimen	Grain Size (μm)
4340 N. P.	12. 5
4340 H. P.	30
18Ni N. P.	12
18Ni H. P.	10

Table V

Crack Orientation

β °	θ °	P kg (lb)	K MPa-$m^{\frac{1}{2}}$ (ksi-$in^{\frac{1}{2}}$)
0	0	251 (551)	17.6 (16.0)
8	-15	255 (560)	17.8 (16.2)
10	-17	256 (563)	17.9 (16.3)
14	-21	260 (570)	18.0 (16.4)
30	-39	285 (627)	20.0 (18.2)
60	-59.5	475 (1044)	33.3 (30.3)
80	-73.0	1415 (3112)	99.3 (90.3)

Table VI

Average Inclusion Spacing or Fracture Process Zone Size (d_T) : μm

Material		Magnification			$\bar{d}^*$	$\bar{d}$
		1500x	3000x	6000x		
AISI 4340 Steel	Normal Purity	7.84	4.97	5.54	6.74 ± 1.89	6.60 ± 1.84
	High Purity	12.39	5.90		8.82 ± 3.58	9.65 ± 3.55
18Ni Maraging Steel	Normal Purity	6.33	5.03		5.49 ± 1.01	6.03 ± 1.10
	High Purity	8.31	6.53		7.60 ± 1.25	7.94 ± 1.23

$$\bar{d}^* = \sum d_{Ti}/n$$

$$\bar{d} = (\sum A_i / \sum N_i)^{\frac{1}{2}}$$

N_i : Number of Inclusions in a Area

A_i : Area

n : Number of Areas Examined

REFERENCES

1. R. P. Wei, S. R. Novak and D. P. Williams, Materials Research and Standards, Vol. 12, No. 9, Sep. 1972, p. 27.

2. S. K. Banerji, C. J. McMahon, Jr., and H. C. Feng, Metallurgical Transactions A, Vol. 9A, Feb. 1978, pp. 237-243.

3. K. Yoshino and C. J. McMahon, Jr., Metallurgical Transactions, Vol. 5, Feb. 1974, pp. 363-370.

4. A. J. Baker, F. J. Lanta and R. P. Wei, Relationships between Microstructure and Toughness in Quenched and Tempered Ultrahigh-strength Steels, ASTM, STP 370, pp. 3-29.

5. A. J. Birkle, R. P. Wei and G. E. Pellissier, Transactions Quarterly, Vol. 59, No. 4, Dec. 1966, pp. 981-990.

6. J. M. Krafft, Correlation of Plain Strain Crack Toughness with Strain Hardening Characteristics of a Low, a Medium, and a High Strength Steel, Applied Materials Research, April 1964, pp. 88-101.

7. J. D. Landes and R. P. Wei, Journal of Engineering Materials and Technology, Vol. 95, Series H, No. 1, Jan. 1973, pp. 2-9.

8. G. W. Simmons, P. S. Pao and R. P. Wei, Metallurgical Transactions A, Vol. 9A, Aug. 1978, pp. 1147-1158.

9. Effect of Purity on Reliability Characteristics of High-Strength Steel, 1st-4th Interim Technical Report, U. S. Steel Corporation Research Laboratory.

10. W. K. Wilson, Westinghouse Research Laboratory, Rpt. No. 67-707-BTLPV-R1, 1967.

11. O. Jonas, Corrosion, 29, 1973, p. 299.

12. W. F. Brown, Jr., and J. E. Srawley, Plain Strain Crack Toughness Testing of High Strength Metallic Materials, ASTM STP 410, 1967.

13. J. D. Landes, Kinetics of Sub-Critical Crack Growth and Deformation in a High Strength Steel, Ph.D. Dissertation, Lehigh University, 1970.

14. J. D. Landes and R. P. Wei, International Journal of Fracture Mechanics, 9, 1973, p. 277.

15. R. P. Gangloff, Gaseous Hydrogen Embrittlement of High Strength Steel, Ph.D. Dissertation, Lehigh University, 1974.

16. A. Sacena and S. J. Hudak, Jr., Westinghouse Research and Development Center, 77-9E7-AFCGR-P1, May 1977, p. 13.

17. S. A. Stern, J. T. Mullhaupt, R. A. Hempstreet and F. S. DiPaolo, Journal of Vacuum Science and Technology, 2, 1965, p. 165.

18. I. M. Bernstern, Metallurgical Transactions, Vol. 1, 1970, p. 3143.

19. M. L. Wayman and G. C. Smith, Metallurgical Transactions, Vol. 1, 1970, p. 1189.

20. B. B. Rath and I. M. Bernstein, Metallurgical Transactions, Vol. 2, 1972, p. 2845.

21. I. M. Bernstein, Materials Science and Engineering, Vol. 6, 1970, p. 3143.

22. G. C. Sih, Methods of Analysis and Solutions of Crack Problems, Noordhoff International Publishing Leyden.

23. R. Viswanathan and S. J. Hudak, The Effect of Impurities and Strength Level on Hydrogen-Induced Cracking in 4340 Steels, Westinghouse Research Laboratory.

24. W. W. Gerberich and F. J. Lessar, Metallurgical Transactions, Vol. 7A, 1976, p. 953.

25. C. S. Carter, Corrosion, Vol. 25, No. 10, 1969, pp. 423-431.

26. P. S. Pao and R. P. Wei, Scripta Metallurgical, Vol. 11, 1977, pp. 515-520.

27. R. P. Gangloff and R. P. Wei, Scripta Metallurgical, Vol. 8, 1974, p. 661.

28. H. G. Nelson, D. P. Williams and A. S. Tetelman, Metallurgical Transactions, 2, 1971, p. 953.

29. D. C. Baird, An introduction to Measurement Theory and Experiment Design, Prentice-Hall, 1962, pp. 48-68.

APPENDIX I

Application of the Electrical Potential Technique to WOL Specimens

An ac electrical potential system was employed for monitoring crack growth. The use of WOL specimens in the current study, as dictated by experimental considerations, requires an experimental calibration of the electrical potential system for measuring crack length for this specimen geometry. A precision grid, consisting of forty lines spaced at 0.05 cm intervals, was photographically etched onto polished WOL specimens of AISI 4340 steel. The crack in each specimen was extended from EDM notch by fatigue loading in an MTS test machine. The electrical potential (V) was continuously monitored on a strip chart recorder. The potential value at each instant in time when the crack intersected a grid line (as visually monitored with 10X telescope) was noted. Data from replicate calibration experiments are presented in Figure A1 as visually measured crack length (a) (corrected aposteriori for crack tunneling[†]) versus the

---

[†]To account for crack tunneling, the "actual" crack length measured to this point was taken equal to the quantity $\frac{2a + b + c}{4}$ where a, b and c are the distances from the loading line to respectively the points A, B and C, as shown in Fig. A1.

normalized potential V* ($V^* = (V-V_r)/V_r$). The reference potential (V_r) was arbitrarily chosen at a crack length sufficiently removed from the EDM notch to minimize the influence of the notch.

A second degree polynomial was fitted to the data in Figure A2 by a least squares technique which minimized errors in visually measured crack length, Equation(A1).

$$a = 1.529 + 4.724\ V^* - 1.225\ V^* \qquad (A1)$$

where a = crack length

$V^* = (V-V_r)/V_r$

V = measured potential

V_r = reference potential corresponding to a crack length of 1.529 cm (0.602 in)

The derivative of this calibration is used to relate crack growth rate to the rate of change of electrical potential Equation (A2).

$$\frac{da}{dt} = (4.724 - 2.449\ V^*)\ \frac{1}{V_r}\ \frac{dV}{dt} \qquad (A2)$$

Equation (A2) agreed to within 1% within an expression for da/dt obtained by numerical differentiation of (V*,a) data. The uncertainty associated with the crack length-potential calibration expression is less than ±1% due to an uncertainty of 0.005 cm in visual measurement of crack length. Use of the crack length correction procedure to modify a values predicted by Equation (A1) increased the uncertainty to ±3% [14]. An uncertainty of ±0.005 cm in

crack length measurement over a 0.05 cm interval translates to an estimated error of ±20% in crack growth rates. This estimated uncertainty in rate is in excellent agreement with statistical analysis of the calibration data population which revealed that the predicative precision of Equation (A3) was ±18% on a 95% confidence level. Correction of rate values inferred from Equation (A3) by crack length shorting procedure introduced an error estimated to be about 20%.

APPENDIX II

Application of the Constant Displacement Control to Modified WOL Specimen

The use of constant displacement control in this study, using a clip gage to measure the crack opening displacement (COD), requires an experiment calibration of the displacement for measuring crack length for this modified WOL specimen geometry, Equation (A4). An analytical relationship between the COD (V), load (P) and crack length (a) has been given by Hudak, et al. [16], and was used as an analytical calibration curve Equation (A4).

$$\frac{a}{W} = f(U) = 1.002037 - 5.1122U + 39.4312U^2 - 751.191U^3 + 4929.57U^4 - 10464.7U^5 \qquad (A4)$$

$$U = [(\frac{BEV}{P})^{\frac{1}{2}}+1]^{-1}$$

A comparison between the predicted crack length and experimentally measured crack length is shown in Fig. A3. This comparison indicates an apparent systematic error of up to 4%, which is likely to be the result of differences in gage location, elastic modulus, etc. A correction for this error is made on the basis of the initial and final crack length for each specimen using a linear correction scheme.

Estimates of uncertainties with this technique can be made using standard methods [29]. If one retains the 4% systematic error as an upper estimate of both systematic and random errors on crack length and assume an uncertainty in load of about 1%, the estimated uncertainty in K_{th} is then ±15%. Most of this uncertainty is associated with the influence of uncertainty in crack length on the geometrical factor in the stress intensity factor expression. Through a propagation of error analysis, after correcting for systematic errors, uncertainty in crack growth rate was estimated to be less than ±45% based on estimated uncertainty of ±1% in the measurements of load and crack opening displacements.

VITA

Hsi-Cheng Chu was born in Hu-Nan, China, the son of Chen-Min and Ai-Yüan Liu Chu, on October 8, 1948. He received his primary and secondary education in Tainan, Taiwan. He graduated from Chung Cheng Institute of Technology, with a Bachelor of Science Degree in Mechanical Engineering in August, 1971.

He served in the Chinese army during 1971-1973. He joined the Kwan Chung company of Kaohsiung, Taiwan, in September, 1973. He entered Lehigh University in June 1977 as a graduate student to pursue his graduate studies in the Department of Mechanical Engineering and Mechanics.

Upon completion of his Master's program, the author will return to Taiwan and resume his work in the steel company.

He married the former Yü-Chian Yuan in October 1974.